nature communications

Article

https://doi.org/10.1038/s41467-026-71027-5

Pulmonary fibroblast activation during *Aspergillus fumigatus* infection enhances lung defense via immunomodulation and tissue remodeling

Received: 11 January 2025

Accepted: 10 March 2026

Published online: 31 March 2026

Check for updates

José P. Guirao-Abad[1,2] ✉, Daniel A. Kasprovic[2], Dongseong Seo[2], Mustafa Ozdemir[1,2], Shannon M. Shearer[1], Bo-Yao Wen[3], Jonathan J. Bowden[1], Christina Grisham[1], Yunguan Wang[4], Michael Tranter[3,5], David S. Askew[1] ✉ & Onur Kanisicak[2,5] ✉

Aspergillus fumigatus is the etiologic agent of invasive aspergillosis, a life-threatening fungal pneumonia initiated by the inhalation of conidia into the lung. If the conidia are not cleared, they secrete large quantities of hydrolytic enzymes and toxins as they grow, causing extensive pulmonary damage. Fibroblasts are central mediators of tissue repair in many organs, but their functional response to pulmonary damage caused by *A. fumigatus* remains unexplored. Here, we employ cell lineage tracing, targeted cell ablation, and single-cell RNA sequencing to monitor fibroblast dynamics upon exposure to *A. fumigatus* in immunocompetent and immunosuppressed hosts. We find that a subset of pulmonary fibroblasts becomes activated in an immunocompetent host following a challenge with *A. fumigatus* conidia, initiating a gene expression program with acquired immunomodulatory properties and enhanced extracellular matrix-secreting capacity. Remarkably, targeted ablation of fibroblasts expressing the profibrotic activation marker periostin shows that invasive *A. fumigatus* infection accelerates in the absence of periostin lineage cells, accompanied by aberrant immune infiltration, tissue damage and severe alveolar hemorrhage. These findings uncover a protective immunomodulatory role for fibroblasts in limiting *A. fumigatus*-induced pulmonary injury and emphasize the importance of the pulmonary stroma in host defense against this invasive fungal infection.

Environmental molds such as *Aspergillus fumigatus* commonly disseminate through the release of conidia (spores) into the air, inevitably exposing the lung to potential infectious threats[1]. Among these fungi, *A. fumigatus* stands out as one of the major invasive fungal infections (IFI) of global concern[2]. The outcome of the interaction between *A. fumigatus* and the lung hinges on the host's immune status. While healthy immunocompetent lungs can successfully eradicate the inhaled conidia before they can initiate infection[3], individuals with

[1]Department of Pathology & Laboratory Medicine, University of Cincinnati College of Medicine, Cincinnati, OH, USA. [2]Division of Basic and Translational Science, Department of Emergency Medicine, The Ohio State University Wexner Medical Center, Columbus, OH, USA. [3]Department of Molecular Medicine and Therapeutics, The Ohio State University Wexner Medical Center, Columbus, OH, USA. [4]Division of Pediatric Gastroenterology, Hepatology and Nutrition, Cincinnati Children's Hospital Medical Center, & the Department of Pediatrics, University of Cincinnati, Cincinnati, OH, USA. [5]Dorothy M. Davis Heart and Lung Research Institute, The Ohio State University Wexner Medical Center, Columbus, OH, USA. ✉e-mail: Jose.GuiraoAbad@osumc.edu; askewds@ucmail.uc.edu; Onur.Kanisicak@osumc.edu

mild immunosuppression or those with pre-existing lung structural defects are vulnerable to pulmonary colonization by the fungus. These colonizing infections are generally not invasive, but the constitutive release of fungal hydrolytic enzymes and toxins triggers a cycle of repeated tissue injury and inflammation that may evolve into a long-term condition known as chronic pulmonary aspergillosis[4,5]. In situations of more severe immunosuppression that may arise in transplant patients, the conidia germinate into the invasive hyphal form of the fungus, resulting in a life-threatening infection known as invasive pulmonary aspergillosis (IPA). IPA is characterized by the polarized growth of hyphae across anatomic boundaries, resulting in extensive tissue damage and dissemination to other tissues[4]. Infections caused by *A. fumigatus* are associated with a high rate of morbidity and mortality, even when treated, and the recent emergence of antifungal drug resistance[6] underscores the need for more understanding of mechanisms involved in pulmonary protection.

The frontline of host defense against inhaled *A. fumigatus* spores involves the integrated activity of lung-resident macrophages and dendritic cells, along with recruited inflammatory cells[7–9]. However, little is known about the contribution of pulmonary stromal cells, defined here as support cells that lack hematopoietic, endothelial and epithelial markers, most of which are fibroblasts. Fibroblasts, which are best known for their role in providing structural support to a tissue through the synthesis and remodeling of the extracellular matrix (ECM), are increasingly recognized as a heterogeneous collection of matrix-secreting cells that can shift under pathologic conditions into distinct populations with diverse functionalities[10–12]. However, the dynamics of fibroblast behavior during the *Aspergillus*-host interaction is currently unexplored.

In this study, we genetically traced fibroblast activation using the previously identified activation marker periostin (Postn)[13–16] and investigated the impact of these Postn-lineage ($Postn^{Lin}$) fibroblasts on the pathogenesis of IPA. The findings reveal that pulmonary inoculation of immunocompetent mice with *A. fumigatus* conidia induces *Postn* expression. These $Postn^{Lin}$ cells were identified as members of the stromal fibroblast population by both immunohistochemistry and bulk RNA-sequencing (RNA-seq) and were localized to anatomic sites expected for pulmonary fibroblasts. Although these $Postn^{Lin}$ fibroblasts represented a subset of the stromal cell population, their depletion in an inducible cell ablation model resulted in exaggerated immune infiltration, increased tissue damage, and accelerating mortality during IPA. Singe-cell RNA sequencing (scRNA-seq) of lung stromal cell populations demonstrated that exposure to *A. fumigatus* induced the transient appearance of two clusters of cells characterized by the expression of distinct matrix-preserving genes, as well as pattern-recognition receptors and proinflammatory cytokines and chemokines with well-established roles in host defense against IFI's. Together, these findings reveal that fibroblasts become activated in the presence of *A. fumigatus* and undergo significant transcriptional rewiring toward an inflammatory profile that modulates the immune response, a phenomenon not previously reported in vivo in the context of a fungal challenge. This highlights a dual role for fibroblasts in pulmonary protection against *A. fumigatus*, involving both immunomodulation and ECM preservation.

Results

Collagen deposition is localized at sites of inflammation induced by *A. fumigatus*

To assess the pulmonary response to *A. fumigatus*, we inoculated immunocompetent mice with a non-lethal dose of conidia (strain CEA10) via the oropharyngeal route (OP)[17]. As expected for immunocompetent animals[18], colony-forming unit (CFU) analysis revealed sterilization of most conidia within 72 h (Fig. S1A). Histologic evaluation of lung tissue on day 1 post-inoculation revealed multiple inflammatory foci, which persisted for at least 7 days (Fig. 1A). However, the inflammatory foci were reduced in size on day 7 relative to day 3, suggesting the beginning of a resolution of the inflammatory response concomitant with fungal clearance. GMS-staining on day 1 post-inoculation demonstrated the presence of both conidia and small germlings within the inflammatory foci (Fig. 1B and S1C), which decreased by day 3 and only fungal debris was detected by days 5 and 7 (Fig. S1C). Trichrome staining revealed collagen fibers interspersed between the inflammatory cells on days 1, 3, 5, and 7 post-inoculation (Fig. 1C). Control sections from saline-treated mice are shown in Fig. S1B. We conclude that the accumulation of collagen within inflammatory foci is an initial response to a pulmonary challenge with *A. fumigatus* conidia in immunocompetent animals.

$Postn^{Lin}$ fibroblasts emerge in response to *A. fumigatus*

Detecting increased collagen deposition at sites of the fungus-host interaction implies that *A. fumigatus* stimulates fibroblasts to enhance ECM secretion. Changes in fibroblast activity in the context of tissue injury has been reported in many tissues and is associated with the induction of a gene expression program that modifies the collagen-producing activity of fibroblasts to maintain tissue integrity[19]. The *Postn* gene, which encodes a matricellular protein involved in ECM organization, tissue remodeling, and the regulation of inflammatory cell migration[13–16], is a well-established fibroblast activation marker. Most resident fibroblasts in adult tissues lack *Postn* expression, but they will activate the gene in response to injury[16]. In this study, we used a genetic cell lineage tracing approach to identify fibroblasts in which the *Postn* promoter has been induced in response to *A. fumigatus*.

To monitor *Postn* promoter activity, one *Postn* allele was replaced with a tamoxifen (TAM)-inducible Cre recombinase knock-in Postn-MerCreMer allele ($Postn^{MCM}$) and crossed with a strain that permanently expresses the tdTomato fluorescent reporter allele upon Cre recombination (R26R-tdTomato) (Fig. 2A). These $Postn^{Lin}$-tracing mice were given an initial oral gavage of TAM on day −1 and then inoculated OP with a non-lethal dose of 3×10^7 conidia in saline on day 0 (Fig. 2B). Only sporadic $tdTomato^+$ fluorescence was observed in lung tissue from $Postn^{Lin}$ mice treated with either TAM alone or TAM plus an OP inoculation of saline (Fig. 2C, top two panels and Figure S2A, top 3 panels; arrows highlight $tdTomato^+$ cells), representing background levels. No sporadic tdTomato expression was detected in the $Postn^{Lin}$ mice in the absence of TAM treatment (Fig. S2A, lower left panel), indicating tight control of the reporter gene without Cre recombination. By contrast, robust tdTomato expression within a subset of fibroblasts was apparent in lungs inoculated with conidia from the CEA10 strain of *A. fumigatus* (Fig. 2C, lower left panel and Fig. S2A, lower middle panel). Interestingly, heat-inactivation of the CEA10 conidia induced a similar level of activation to viable conidia, indicating that metabolic activity of the fungus is not required for this response (Fig. S2A, lower right panel). Comparable levels of expression were induced by two other *A. fumigatus* clinical isolates (Af293 and H237), demonstrating that the response is not *A. fumigatus* strain-specific (Fig S2B). No expression was seen in mice inoculated with *A. fumigatus* without TAM treatment, demonstrating robust control of the reporter even with a strong inducer of fibroblast activation (Fig. 2C, lower right panel). TdTomato-expressing activated fibroblasts were detectable histologically on day 3 post-inoculation, with the number of labeled cells peaking on day 7 (Fig. 2D, quantified in 2E), reaching levels that were 100-fold higher, on average, than the sporadic activation observed following OP saline inoculation (Fig. 2F). The optimum dose range required to elicit a detectable activation response was 2-4 x 10^7 conidia administered as a single OP inoculation (Fig. S3). We conclude that the *A. fumigatus*-host interaction in the immunocompetent lung triggers the emergence of a population of fibroblasts characterized by expression of the *Postn* gene.

https://doi.org/10.1038/s41467-026-71027-5

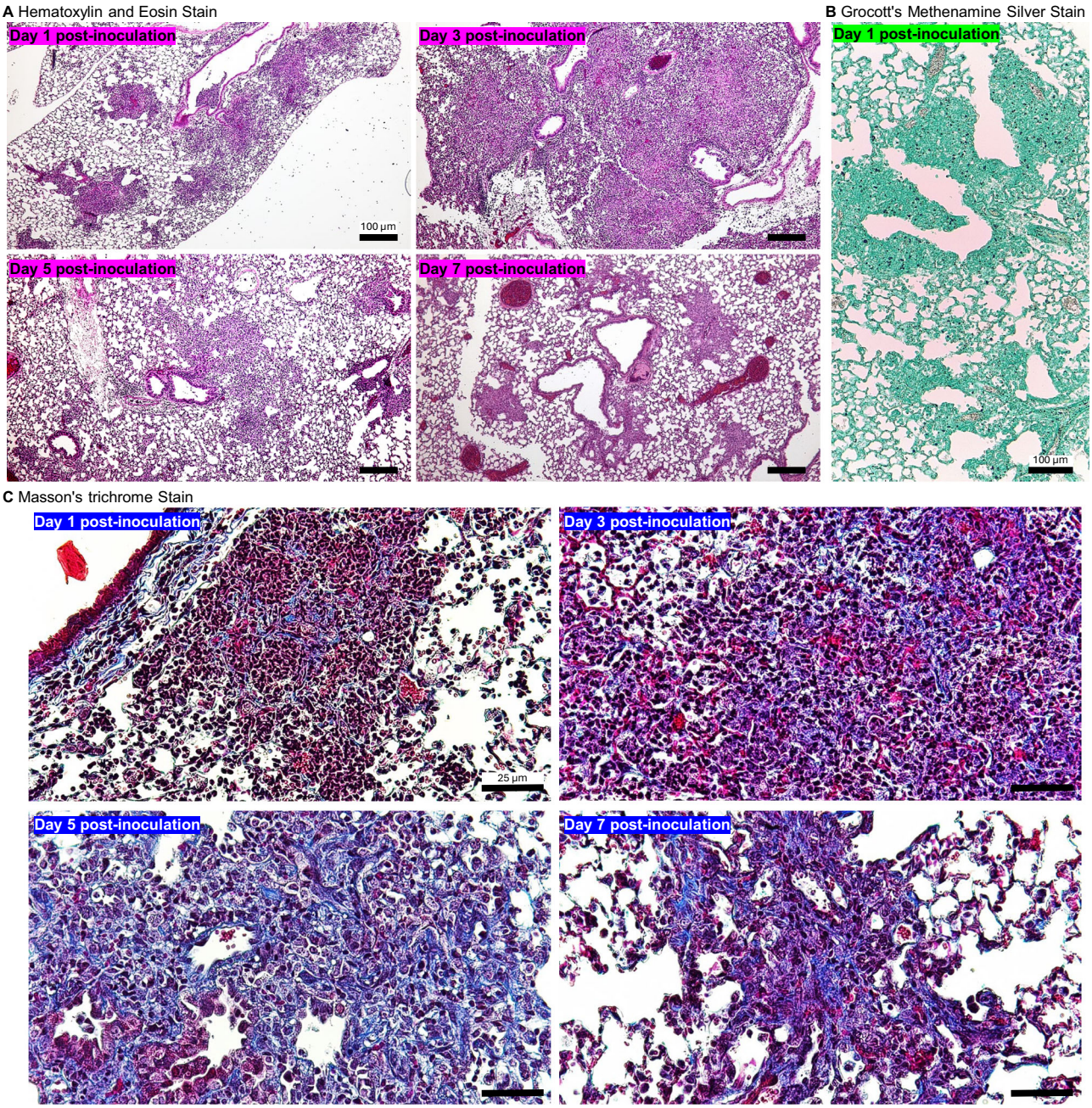

Fig. 1 | Collagen fiber deposition is an initial response to *A. fumigatus*. Representative images of paraffin-embedded lung sections from immunocompetent mice on days 1, 3, 5, and 7 post-inoculation with 3×10^7 *A. fumigatus* conidia. Sections were stained with (**A**) hematoxylin and eosin (H&E), (**B**) Gomori's methenamine silver (GMS) to highlight fungal elements (black), or (**C**) Masson's trichrome to highlight collagen fibers (blue).

Postn^{Lin} fibroblasts induced by *A. fumigatus* are predominantly alveolar

Characterization of pulmonary fibroblast heterogeneity by scRNA-seq has revealed unique molecular profiles for populations of fibroblasts that reside in distinct anatomic sites: directly beneath the epithelial lining of large and small conducting airways (peribronchial fibroblasts), in the connective tissue surrounding bronchovascular bundles (adventitial fibroblasts), or within the alveolar interstitial space between epithelial walls (alveolar fibroblasts)[19]. To determine where Postn^{Lin} fibroblasts localize, we quantified the number of tdTomato$^+$ cells at each site by immunohistochemistry, confirming localization by co-staining with antibodies against epithelial (EpCAM), endothelial (CD31), and smooth muscle (Myh11) markers. The majority of the Postn^{Lin} cells arising 7 days post-inoculation with *A. fumigatus* conidia were found within the alveolar interstitium (Fig. 3B, arrows). A smaller proportion was sandwiched between the bronchiolar epithelium and the underlying smooth muscle (Fig. 3C, enlarged in Fig. 3D), and the fewest Postn^{Lin} cells showed an adventitial localization surrounding perivascular smooth muscle (Fig. 3E, enlarged in Fig. 3F). Quantification of TdTomato$^+$ cells at the three major anatomic sites is shown in Fig. 3A.

Postn^{Lin} cells induced by *A. fumigatus* belong to the fibroblast population

Platelet-derived growth factor α (Pdgfrα) is expressed by most tissue resident fibroblasts and is widely used as a marker for that cell type, including for those found in the lung[11,20]. We therefore used a Pdgfrα lineage (Pdgfrα^{Lin}) tracing mouse to compare the morphology of

https://doi.org/10.1038/s41467-026-71027-5

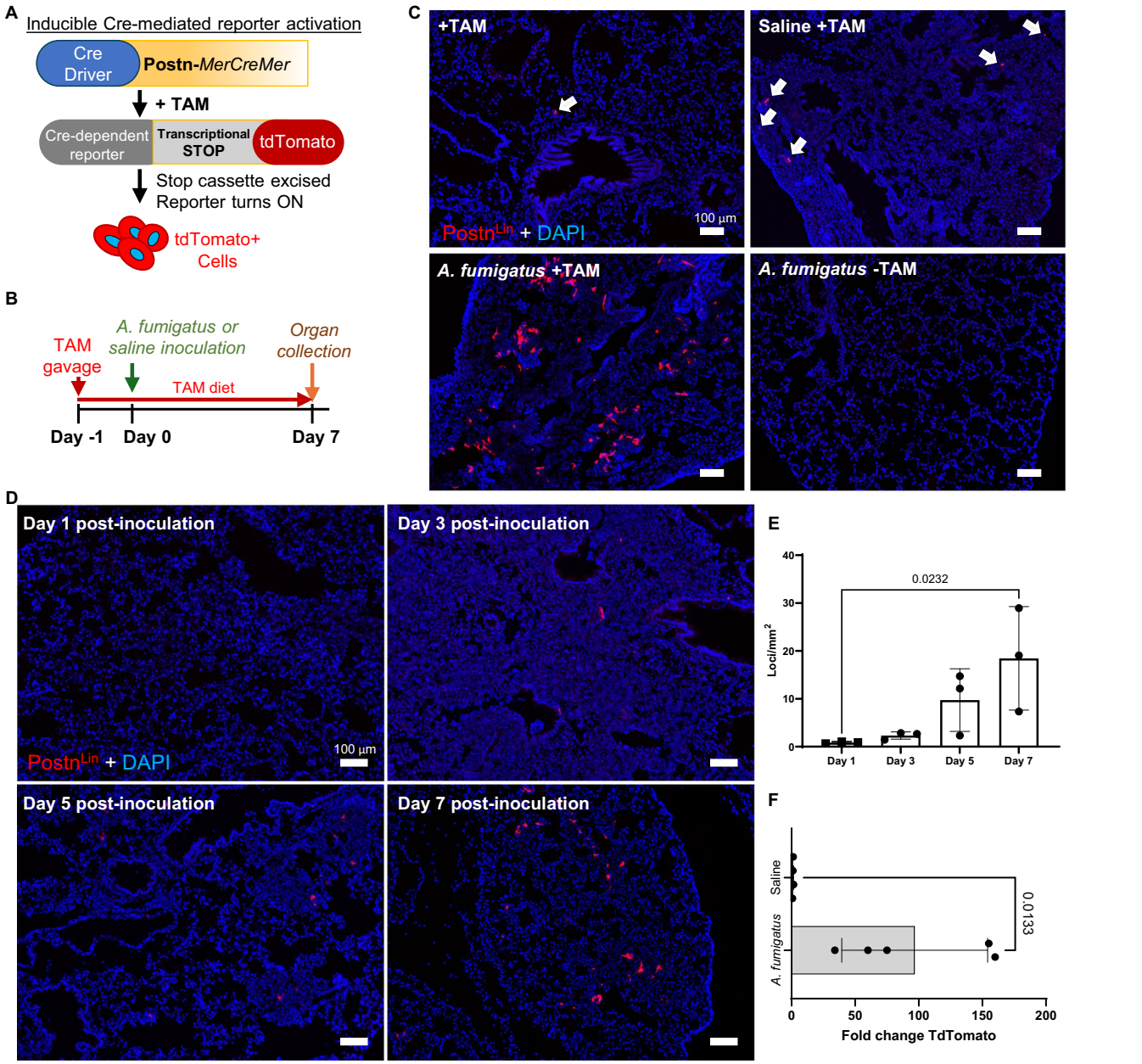

Fig. 2 | Postn^{Lin} cells are induced by *A. fumigatus* in immunocompetent mice. **A** Schematic representation of the TAM-inducible Cre recombinase system. Cre recombinase, flanked by a tamoxifen-inducible modified estrogen receptor (*MerCreMer*), was inserted into the Postn locus, enabling temporal control over Cre activity in cells that activate the *Postn* promoter. In the presence of TAM, Cre translocates to the nucleus and catalyzes recombination between loxP sites flanking a transcriptional stop upstream of a tdTomato reporter gene inserted into the rosa26 locus. Cre activity results in constitutive expression of tdTomato in Cre-expressing cells and their progeny, thereby fluorescently marking Postn^{Lin} fibroblasts. **B** Schematic representation of the experimental approach used to study fibroblast activation in Postn^{Lin} immunocompetent mice after OP inoculation with 3×10^7 *A. fumigatus* conidia. TAM was administered via gavage one day before the fungal challenge and maintained through a TAM-infused chewing diet for the duration of the experiment. **C** Representative fluorescent photomicrographs showing the induction of tdTomato-positive cells following exposure to the specified treatments. Arrows indicate sporadic Postn^{Lin} cells in samples not treated with *A. fumigatus*. **D**, **E** Time course illustrating the appearance of tdTomato$^+$ cells on days 1, 3, 5, and 7 post-inoculation with *A. fumigatus*. Bars represent the means ± SD from 3 biological replicates, each shown as an individual dot (*$p < 0.05$; one-way ANOVA on ranks with Tukey's post hoc test). **F** Flow cytometric analysis of fold-change in tdTomato expression following inoculation with 3×10^7 conidia relative to mock infection with saline. Values represent the means ± SD from 4 and 5 biological replicates in the control and *A. fumigatus*-treated groups, respectively. Dots indicate individual biological replicates (*$p < 0.05$; unpaired two-tailed *t*-test). Source data are provided as a Source Data file.

quiescent Pdgfrα^{Lin} resident pulmonary fibroblasts to that of *A. fumigatus*-induced Postn^{Lin} fibroblasts. Quiescent resident Pdgfrα^{Lin} fibroblasts in untreated mice displayed a thin, elongated morphology and were widely distributed throughout the lung in the same alveolar, peribronchial and adventitial locations as *A. fumigatus* induced Postn^{Lin} cells (Fig. S4A–D). Postn^{Lin} fibroblasts that localized to peribronchial, and adventitial locations showed a similar morphology, but those that were found clustered among regions of inflammation in the alveoli displayed a more hypertrophic and dendritic morphology with numerous branched extensions (Fig. S4E–H). To determine whether Postn^{Lin} cells express the Pdgfrα fibroblast marker, the Postn^{Lin} mice were crossed with a Pdgfrα-GFP mouse in which the endogenous *Pdgfrα* promoter constitutively drives expression of a histone H2B-eGFP fusion protein[21,22]. The resulting Postn^{Lin}/Pdgfrα-GFP strain was

https://doi.org/10.1038/s41467-026-71027-5

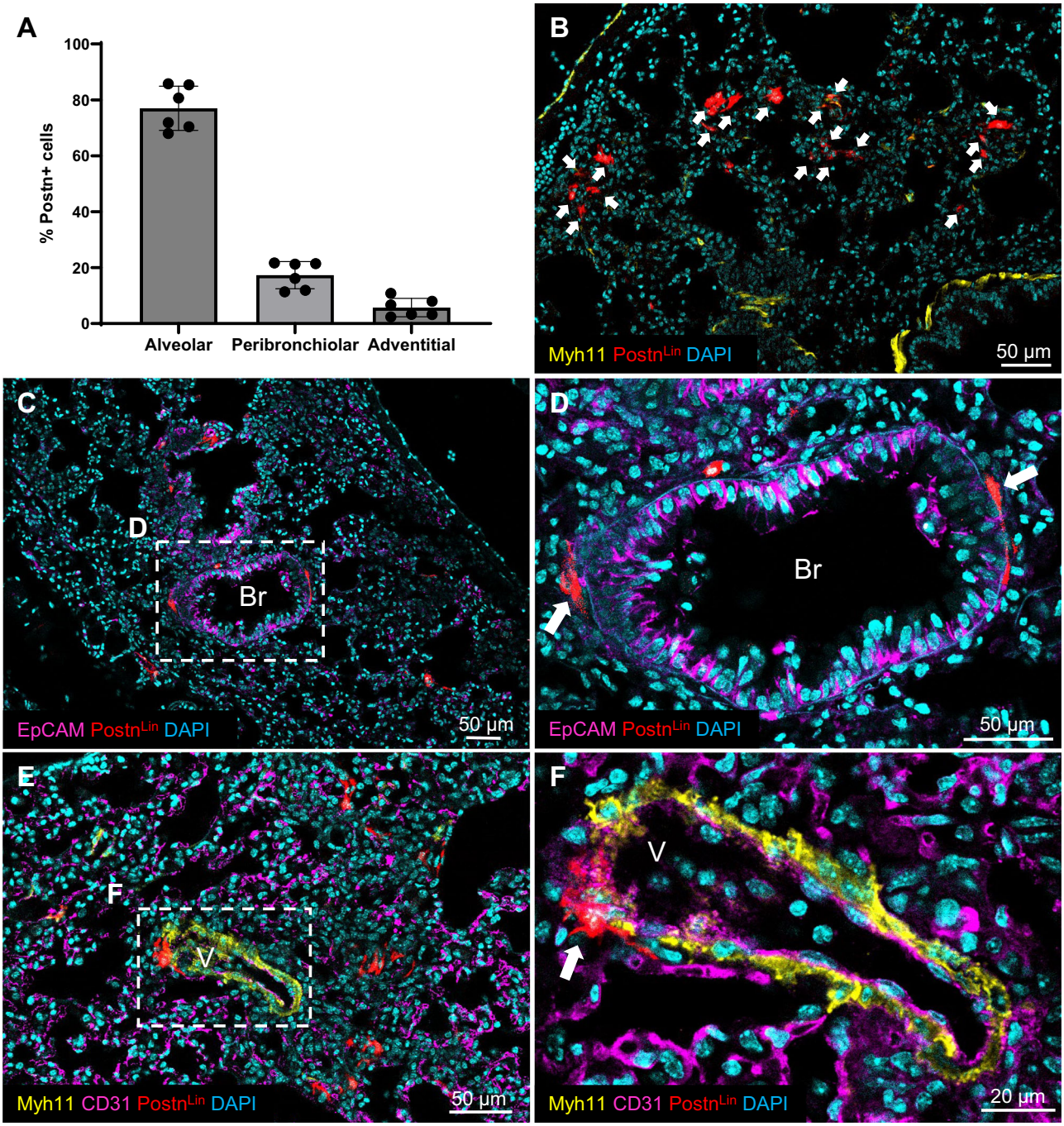

Fig. 3 | Postn^{Lin} cells are predominantly in the alveolar interstitium. **A** Quantification of the proportion of Postn^{Lin} cells in alveolar, peribronchiolar, and adventitial locations by immunohistochemistry. Values represent the mean ± SD from 6 biological replicates, each shown as an individual dot. **B** Representative image of Postn^{Lin} cells in alveolar spaces, highlighted with white arrows. **C** Low-power and (**D**) high-power images of peribronchiolar (Br) localization: arrows point to Postn^{Lin} cells located beneath the bronchiolar epithelium stained with an antibody against the epithelial marker EpCAM. **E** Low-power and (**F**) high-power images of Postn^{Lin} cells in an adventitial location surrounding a vessel (V). Arrow indicates Postn^{Lin} cells underlying the perivascular smooth muscle. Endothelial cells are highlighted using an antibody against CD31, whereas smooth muscle cells are stained with an antibody against Myh11. Source data are provided as a Source Data file.

inoculated with 3×10^7 conidia and examination of lung sections on day 7 post-inoculation revealed a subset of Postn^{Lin} fibroblasts that also expressed Pdgfrα (Fig. 4A–B, green arrows). Quantification by flow cytometry showed that approximately 60% of the tdTomato$^+$ cells co-expressed Pdgfrα (Fig. 4C), similar to what has been previously reported for Postn^{Lin} cells in the heart[11,16,22].

We also found that approximately 25% of the tdTomato$^+$ cells co-stained with smooth muscle myosin heavy chain 11 (Myh11), a marker that is expressed by smooth muscle cells as well as a subset of alveolar fibroblasts that have differentiated to a contractile myofibroblast phenotype[11,23] (Fig. 4D–E, colocalization shown by orange arrows). Most of the observed Myh11$^+$/tdTomato$^+$ colocalization was in alveolar regions where smooth muscle is absent, suggesting that the majority of the double-labeled cells represent contractile myofibroblasts. By contrast, tdTomato$^+$ cells did not co-stain with markers for endothelial cells (CD31, Fig. 4F, G) or epithelial

https://doi.org/10.1038/s41467-026-71027-5

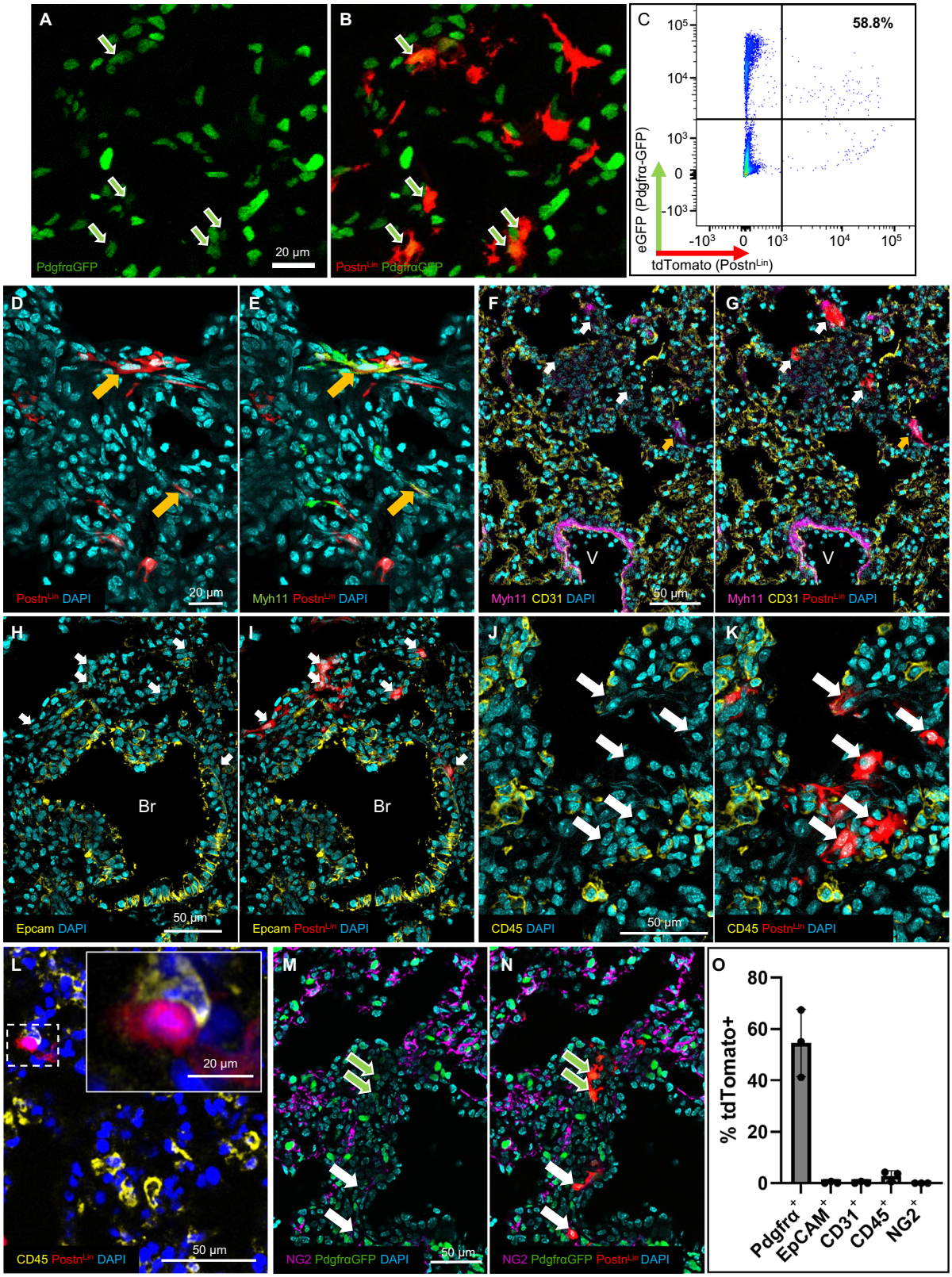

cells (EpCAM, Fig. 4H, I) by immunohistochemistry. Likewise, no co-labeling was observed with the hematopoietic marker CD45 (Fig. 4J–L), although CD45$^+$ cells were frequently found in close proximity to tdTomato$^+$ cells (Fig. 4L, inset). Flow cytometry further confirmed the absence of non-stromal labeling (EpCAM and CD31), showing only minimal tdTomato$^+$/CD45$^+$ populations (Fig. 4O and Fig. S5).

As some studies indicate that pericytes may express periostin, particularly under fibrotic conditions[24] we investigated whether tdTomato$^+$ cells co-express Neuron-Glial Antigen 2 (NG2, encoded by Cspg4), a canonical pericyte marker[25]. Both Flow cytometry and confocal immunohistochemistry analyses of *A. fumigatus*-induced Postn^{Lin} cells revealed no evidence of co-localization between tdTomato$^+$ cells with NG2$^+$ cells (Fig. 4M–O and Fig. S5H). Taken together, these

Fig. 4 | Postn^{Lin} cells belong to the fibroblast population. A, **B** Images display colabeling of Pdgfrα-GFP (green nuclei) with *A. fumigatus*-induced Postn^{Lin} cells (red cells), highlighted by green arrows. **C** Representative flow cytometry plot showing tdTomato$^+$ cells (rightward scatter) against Pdgfrα cells (upwards scatter). The percentage of Pdgfrα$^+$ cells within the tdTomato$^+$ population is depicted in the upper right quadrant. **D**, **E** Images show Postn^{Lin} cells and Myh11-labeled cells, with DAPI-stained nuclei in blue. Orange arrows show co-staining. **F**–**K** Representative images showing the lack of colocalization between Postn^{Lin} cells and antibody staining against the endothelial marker CD31 (**F**, **G**), the epithelial marker EpCAM (**H**, **I**), the hematopoietic marker CD45 (**J**–**L**), and the pericyte marker NG2 (**M**, **N**). The color coding is shown at the base of the figure. Arrows highlight the location of Postn^{Lin} cells to facilitate the comparison of colocalization: white arrows denote lack of co-staining, orange arrows indicate colocalization with Myh11, and green arrows highlight colocalization with PdgfraGFP. The inset in panel L represents an example of how Postn^{Lin} cells are often observed in close contact with hematopoietic cells. **O** Flow cytometric quantification of tdTomato$^+$ cells colabeled with markers for fibroblasts (Pdgfrα), smooth muscle (Myh11), epithelial cells (EpCAM), endothelial cells (CD31), hematopoietic cells (CD45), and pericytes (NG2). Values represent the mean ± SD from 3 biological replicates, each shown as an individual dot. Source data are provided as a Source Data file.

findings indicate that Postn^{Lin} cells induced by *A. fumigatus* in the lung belong to the pulmonary fibroblast population and exhibit an activated state and morphology distinct from resident Pdgfrα^{Lin} fibroblasts.

Postn^{Lin} cells express a unique transcriptional profile of matrix modification compared to resident pulmonary fibroblasts

To assess how the *A. fumigatus*-host interaction impacts gene expression in the stromal population, we performed bulk RNA-seq on *A. fumigatus*-induced Postn^{Lin} fibroblasts, using resident Pdgfrα-GFP fibroblasts as the comparator. Immunocompetent Postn^{Lin} mice were administered a single inoculum of *A. fumigatus* conidia to induce fibroblast activation and Pdgfrα-GFP mice were given a mock inoculation with saline. The induced Postn^{Lin} cells and the resident Pdgfrα-GFP fibroblasts were then isolated on day 7 post-inoculation by sorting tdTomato$^+$ or GFP$^+$ cells that were negative for vascular (CD31), epithelial (EpCAM), and hematopoietic (CD45) markers (see Fig. S6 for sorting strategy). Total RNA was extracted from the two populations and bulk RNA-Seq was performed to compare the transcriptional profile of *A. fumigatus*-induced Postn^{Lin} cells to that of Pdgfrα$^+$ resident fibroblasts.

A total of 1037 differentially expressed genes (DEGs) were identified using a statistical cutoff of a Bonferroni-adjusted P-value ≤ 0.05 and a fold change greater than ± 1.5 (Fig. 5A; Data S1). Among these DEGs, 552 were upregulated in the Postn^{Lin} population while 485 were downregulated, which are highlighted in the volcano plot shown in Fig. 5A. Genes involved in ECM organization, cell adhesion, and angiogenesis were among the top 10 enriched Gene Ontology (GO) terms in both the upregulated and downregulated categories (Fig. 5B–C; Data S2 and S3), demonstrating that the tissue remodeling activity of Postn^{Lin} fibroblasts is distinct from that of resident pulmonary fibroblasts. Downregulated genes were enriched in GO categories associated with signaling pathways, metabolism, gene expression, cell differentiation and proliferation (Fig. 5C; Data S3) reflecting the comprehensive transcriptional rewiring that is necessary for resting fibroblasts to transition to an activated phenotype. Several of the genes that were downregulated in response to *A. fumigatus* represent markers of resident pulmonary fibroblasts, including *Pdgfrα*, *Tcf21*, and *Scube2*[26] (Fig. 5D), suggesting that pathogen exposure induces a shift away from the gene signature of resident fibroblasts.

Among the top upregulated DEGs were those involved in fibroblast activation and fibrosis (selected genes are highlighted in Fig. 5D). These include: Grem1 (Gremlin1), a bone morphogenic protein agonist involved in ECM regulation and fibrosis[27,28]; *Cthrc1* (collagen triple helix repeat containing 1), a secreted ECM component implicated as the major effector of fibrotic processes in the injured lung[26]; *Actg2* (actin gamma 2), linked to fibroblast activation in the lung[29]; *IBSP* (integrin binding sialoprotein (IBSP), identified in fibrotic lungs[30]; and *Lrrc15* (leucine-rich repeat containing 15), associated with myofibroblast populations[31–33]. Additional DEGs previously reported to be associated with fibrotic fibroblast activity included *Myh11*, *Tagln*, *Tpm2*, *Acta2*, *Des*, *Col1a1*, *Col1a2*, *Col5a1*, *Spp1*, *Ltbp2*, *Tnc* and *Igfbp2*[26,29] (Fig. 5D). These results suggest that rewiring of fibroblast gene expression to modify the ECM is central to confronting an infectious threat from *A. fumigatus*, consistent with our observation of collagen accumulation within inflammatory foci in the lung induced by *A. fumigatus* (Fig. 1C).

Targeted ablation of the Postn^{Lin} lineage exacerbates the severity of invasive pulmonary aspergillosis

To investigate the impact of Postn^{Lin} cells on IPA pathogenesis, we employed a conditional cell ablation model in which a TAM-inducible *Postn^{MCM}* mouse was crossed to a recombinase-responsive diphtheria toxin subunit A (DTA)[34] expressing mouse line (Fig. 6A). In this approach, fibroblasts activating the *Postn* promoter express DTA, thereby selectively killing the cells and preventing fibroblast activity and downstream responses. IPA was induced using a modified triamcinolone-based immunosuppression protocol[35]. After inoculating mice with 1×10^6 conidia the host-pathogen interaction was allowed to occur for 5 h without immunosuppression, after which a single dose of triamcinolone acetonide was administered for immunosuppression, and the progression of IPA was monitored over time (Fig. 6B). Control mice received saline as a mock inoculation.

Infected DTA mice exhibited accelerated mortality relative to controls (Fig. 6C), accompanied by hemoptysis and evidence of gross pulmonary hemorrhage in dissected lungs (Fig. 6D). Histopathology revealed focal alveolar hemorrhage with extensive fungal angioinvasion (Fig. 6E). Quantitative scoring of histologic sections demonstrated higher levels of alveolar hemorrhage and angioinvasion in DTA mice compared to controls (Fig. 6F–G; Figure S7). To determine whether a major loss in ECM could have predisposed to alveolar hemorrhage and angioinvasion, we assessed collagen deposition and organization by Picrosirius Red staining. As expected, collagen was present within the inflammatory foci, but overall content was not reduced following Postn^{Lin} ablation, suggesting that vascular rupture was not due to a gross structural loss of collagen support (Fig. 6H).

To exclude the possibility that the differences in mortality observed in the DTA/Cre model were independent of IPA, we challenged immunocompetent mice with a high dose inoculum of 3×10^7 *A. fumigatus* conidia. *Postn$^{MCM/+}$*; R26-DTA and control mice were administered tamoxifen one day prior to OP inoculation with *A. fumigatus* conidia and were maintained on tamoxifen chow until day 14 post-infection for effective recombination[36–38] (Figure S8A). In contrast to the IPA model, no significant difference was observed between the two groups (Fig. S8B), indicating that IPA is necessary to elicit accelerated mortality in the DTA background. To determine whether fibroblast ablation impacts vascular integrity in the absence of IPA, fluorescently labeled dextrans of various sizes were administered into the lung at day 4 post-infection, and their subsequent appearance in the circulation was quantified. Fibroblast ablation had no detectable impact on the appearance of dextrans in the circulation (Fig. S8C), indicating that vascular permeability in the immunocompetent lung was unaffected by conditional ablation of Postn^{Lin} cells.

The two major drivers of tissue injury and mortality during IPA are fungal burden and immune-mediated tissue damage[39,40]. Fungal burden was assessed by qPCR analysis of lung tissue prior to the first observed deaths on day 4 (Fig. 6I). Flow cytometry confirmed effective fibroblast depletion, with ~30% fewer viable Pdgfrα$^+$ cells in *Postn$^{MCM/+}$*; R26-DTA lungs relative to controls (Fig. 6J). Fungal burden was

https://doi.org/10.1038/s41467-026-71027-5

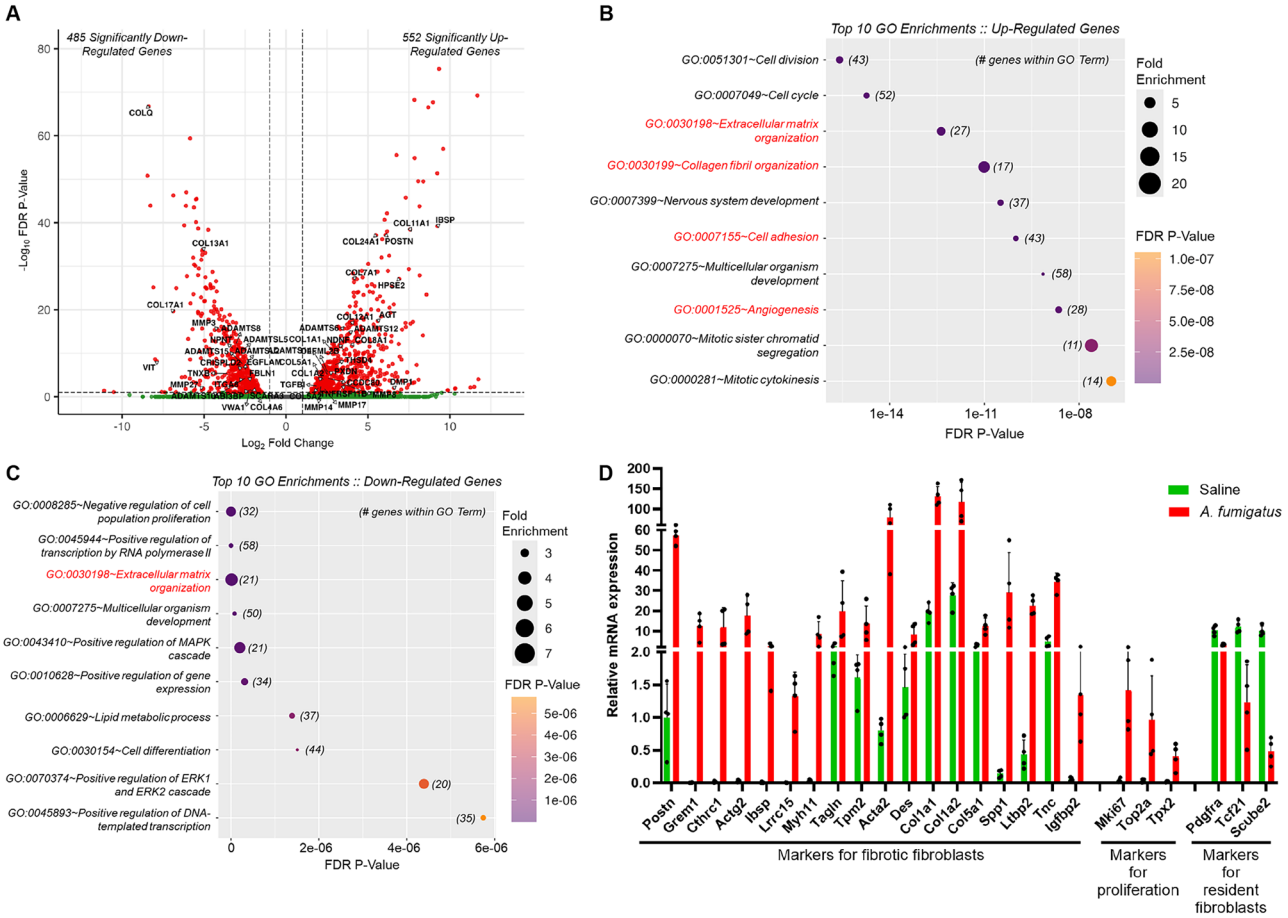

Fig. 5 | Postn^{Lin} cells express a unique transcriptional profile of ECM modification compared to resident pulmonary fibroblasts. Induced Postn^{Lin} cells and resident Pdgfrα^{Lin} fibroblasts were isolated by flow cytometry as described in methods and total RNA was sequenced. **A** Volcano plot shows 485 down-regulated and 552 up-regulated genes after *A. fumigatus* infection. Genes related to extracellular matrix organization (GO:0030198) are highlighted. Top 10 *A. fumigatus*-dependent GO Terms for significantly (**B**) upregulated and (**C**) downregulated genes, ranked by P-value and fold enrichment. Matrix remodeling terms are highlighted in red. **D** Expression comparison of selected differentially expressed genes between *A. fumigatus*-induced Postn^{Lin} cells and mock-treated Pdgfrα^{Lin} cells. Values represent the means ± SD from 4 biological replicates. Dots indicate individual biological replicates. Differential gene expression was assessed using DESeq2 with two-sided Wald tests, and *P*-values were adjusted for multiple comparisons using the Benjamini–Hochberg false discovery rate (FDR) method. Source data are provided as a Source Data file.

equivalent between groups, ruling out pathogen overload as the cause of worsened outcomes and accelerated mortality (Fig. 6K).

In this transient immune suppression model of IPA, immune reconstitution by day 4 post-inoculation is known to contribute to pulmonary damage and mortality[41]. To determine whether fibroblast ablation impacts the extent of immune cell migration into lung tissue, distinct cellular subsets were quantified by flow cytometry. As anticipated, myeloid recruitment into the lung was evident in both control and DTA-ablated mice; however, DTA mice exhibited a striking increase in macrophages, along with elevated numbers of neutrophils, dendritic cells, eosinophils, and NK cells, while basophils, B and T cell numbers remained unchanged (Fig. 6L). We conclude that the loss of Postn^{Lin} cells in the context of IPA is associated with accelerated mortality and a dysregulated innate immune response to *A. fumigatus*, accompanied by pathological features consistent with vascular injury and fungal invasion.

Pulmonary fibroblast sub-populations with enhanced matrix stabilizing and immunomodulatory characteristics emerge following a challenge with *A. fumigatus*

Although immune cell infiltration was increased following Postn^{+} cell ablation, immunological functions for fibroblasts were not enriched among the top GO terms in the bulk RNA-seq analysis. This RNAseq analysis was performed at day 7 post-inoculation, coinciding with the peak accumulation of tdTomato^{+} fibroblasts (Fig. 2D–E), and revealed a predominant gene expression signature of matrix-modifying activity. Importantly, the Postn^{Lin} population sequenced at this time point includes all cells that activated the *Postn* promoter during the preceding week, leading to permanent tdTomato labeling of both the initially activated fibroblasts and their progeny. Thus, the dataset reflects an averaged transcriptomic profile, encompassing newly activated fibroblasts as well as cells transitioning toward alternative functional states or returning to a quiescent phenotype. To determine whether fibroblasts with immune characteristics emerge at earlier stages of the host-fungal interaction and to delineate other potentially important subsets of fibroblasts that could be masked by averaging major populations, we used single-cell RNA-sequencing (scRNA-seq). Immunocompetent mice were exposed to either a single inoculum of conidia or a mock inoculation with saline. The stromal cell population was then isolated from total lung cells on days 1 and 7 post-inoculation by flow cytometry, excluding the non-stromal population based on expression of CD31, CD45 and EpCAM, consistent with the bulk RNA-seq analysis (Fig. 7, see Fig. S6 for sorting strategy). The resulting stromal cell population was then subjected to a single-cell transcriptome analysis.

Cell typing was performed using unsupervised clustering and a reference scRNA-seq dataset of pulmonary fibroblast populations[19].

https://doi.org/10.1038/s41467-026-71027-5

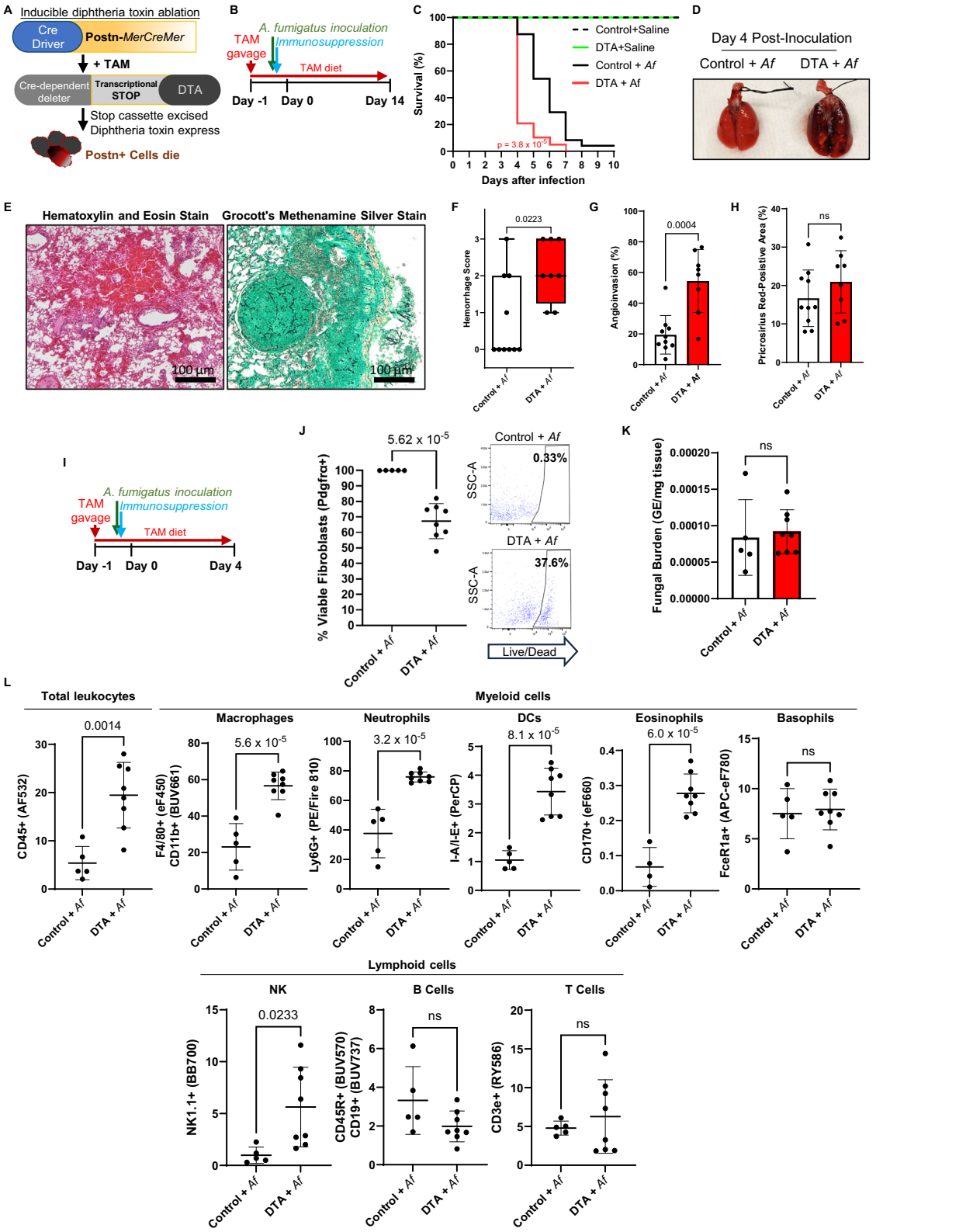

This approach identified 9 distinct stromal populations (Fig. 7B and Fig. S9), with clusters 1 and 2 classified as alveolar fibroblasts, cluster 3 as peribronchial fibroblasts, cluster 4 as pericytes, cluster 5 as adventitial fibroblasts, clusters 6-8 as *A. fumigatus*-induced clusters (highlighted by the asterisks), and cluster 9 as an indistinct population of fibroblasts with mixed characteristics. Representative genes used for cell typing are shown in Fig. 7C. As expected, *Pdgfra*$^{+}$ cells were distributed across multiple clusters, consistent with the experimental enrichment of a stromal fibroblast population. *Scube2*$^{+}$ cells, representing an alveolar fibroblast phenotype, were distributed across 4 clusters (Fig. 7B: clusters 1, 2, 6 and 7); *Hhip*$^{+}$/*Cd9*$^{+}$ cells, indicative of peribronchial fibroblasts, were present in 2 clusters (Fig. 7B: clusters 3 and 8); *Ly6a*$^{+}$/*Cd9*$^{+}$ cells, indicating adventitial fibroblasts were located in cluster 5 (Fig. 7B); and cluster 4 was marked by the pericyte marker

Fig. 6 | Targeted ablation of Postn^{Lin} cells accelerates the progression of IPA by exacerbating immune infiltration and tissue damage. A Schematic of the TAM-inducible DTA ablation model. The Cre recombinase, inserted into the Postn locus, is controlled by a TAM-inducible estrogen receptor (*MerCreMer*). Upon *Postn* promoter activation, TAM-induced recombination of the DTA gene results in DTA toxin expression from the rosa26 locus, preventing fibroblast activation and expansion. **B** Schematic representation of the experimental approach: Mice were inoculated OP with 1×10^6 conidia, followed by immunosuppression with triamcinolone acetonide 5 h post-infection. TAM was administered via gavage one day before fungal inoculation and maintained through a TAM-infused chewing diet for the duration of the experiment. **C** Percent survival of immunosuppressed mice infected with *A. fumigatus* ($n = 24$ for control group and $n = 20$ for DTA group; $p = 3.8 \times 10^{-5}$, log rank test). **D** Gross appearance of lungs from infected DTA and control mice on day 4 post-infection. **E** Representative histopathologic images showing focal alveolar hemorrhage and angioinvasion in the *A. fumigatus*-infected DTA mice by H&E and GMS staining, respectively. **F** Distribution of alveolar hemorrhage severity in control (white bars) and DTA mice (red bars). Alveolar hemorrhage was scored semi quantitatively as described in Fig. S7. Data are shown as box-and-whisker plots with individual biological replicates overlaid ($n = 10$ for control group and $n = 8$ for DTA group). Boxes represent the interquartile range (IQR), horizontal lines indicate the median, and whiskers extend to 1.5 x IQR (two-tailed Mann–Whitney *U* test). **G** Quantification of angioinvasion in intrapulmonary arteries of control (white bars) and DTA (red bars) mice. The percentage of vessels ≥100 μm in diameter that contained *A. fumigatus* hyphae in each animal were quantified in GMS-stained lung sections. Values represent the mean ± SD from 10 and 8 biological replicates in the control and DTA groups, respectively, with individual replicates indicated by dots (unpaired two-tailed *t*-test). **H** Collagen deposition quantified from Picrosirius Red-stained sections of lung tissue. Values represent the mean ± SD from 10 and 8 biological replicates in the control (white bars) and DTA (red bars) groups, respectively, with individual replicates indicated by dots (ns, no significant; unpaired two-tailed *t*-test) (**I**) Schematic representation of the experimental approach: similar to the schematic shown in (**B**), but lung tissue was harvested at day 4 post-challenge for further analysis, coinciding with the highest mortality rate observed in (**C**). **J** Flow cytometric quantification of viable Pdgfrα$^+$ cells. Right panels show the cell gating strategy used to distinguish viable and dead cells within the Pdgfrα$^+$ population. Values represent the mean ± SD from 5 and 8 biological replicates in the control and DTA groups, respectively ($p = 3.5 \times 10^{-5}$; unpaired two-tailed *t*-test). **K** Fungal burden quantification by RT-qPCR from lung lobes of the indicated mouse models. Fungal burden is expressed as Genome Equivalents (GE) per mg of lung tissue. Values represent the mean ± SD from 5 and 8 biological replicates in the control (white bars) and DTA (red bars) groups, respectively, with individual replicates indicated by dots ($p < 0.05$; unpaired two-tailed *t*-test). **L** Quantification of immune infiltration by flow cytometry. Total leukocytes and hematopoietic subsets were discriminated using the antibodies indicated on the *y*-axis. Values represent the mean ± SD from 5 and 8 biological replicates in the control and DTA groups, respectively, with individual replicates indicated by dots (ns, no significant, unpaired two-tailed t-test). Source data are provided as a Source Data file.

Cox4i2 (Fig. 7B). Cells in the alveolar and peribronchial fibroblast clusters in the saline-inoculated mice (Fig. 7D–E, left panel) reduced in number in response to *A. fumigatus* on day 1 post-infection (Fig. 7D–E, middle panel), coinciding with the appearance of an activated alveolar fibroblast cluster (Activated^{Alv}) and an activated peribronchial fibroblast cluster (Activated^{Pbr}, purple and red clusters, respectively).

Analysis of the differentially expressed genes (DEGs) contained within the various activated fibroblasts identified unique and overlapping genes that fell into two notable categories: ECM synthesis and immune modulation (Data S4-5). In the ECM category, both activated clusters were enriched for genes involved in the formation of matrix structural fibers, encoding 9 different types of collagen, as well as elastin, fibrillin, and three secreted lysyl oxidase enzymes with roles in the formation of collagen and elastin crosslinks that stabilize the ECM[42–44] (Data S4). In addition, several genes encoding integrins that represent the main cellular receptors used to interact with proteins in the ECM were shared between both clusters. In many organs, the TGFβ regulatory system plays a central role in driving de novo collagen synthesis[42]. This fibrogenic function of TGFβ is transduced by the cytosolic signaling protein Smad3 and is tightly regulated by latent TGFβ binding protein 1 (ltbp1), which sequesters TGFβ in the ECM. The observed enrichment of *TGFβ*, *ltbp1*, and *Smad3* in the activated alveolar fibroblast cluster is therefore consistent with a predominant fibrogenic role for these cells (Data S4). This cluster was also remarkable for the presence of 16 DEGs encoding matrix-modifying proteins, indicating that its component cells were actively engaged in remodeling the ECM[45]. The expression of α-smooth muscle actin (*Acta2*) was notably upregulated in the activated peribronchial cluster, suggesting that some of these cells had differentiated to a contractile myofibroblast phenotype[46].

The second group of DEGs in the activated clusters were associated with immune modulatory activity (Data S4), particularly in the activated alveolar fibroblast population. These included the cytokines IL-6, IL-10, and IL-11, as well as multiple cytokines that are members of the TNF, TGFβ, and BMP superfamilies (Data S4). The presence of TGFβ is particularly significant because of its dual role in regulating immune responses as well as fibrogenesis[42]. Although first-line defense against *A. fumigatus* relies heavily on tissue-resident alveolar macrophages and dendritic cells, additional inflammatory cells such as neutrophils, inflammatory monocytes, and monocyte-derived dendritic cells are recruited to the site of infection as needed[47]. The signal that brings these cells into the lung involves the secretion of chemokines[47]. Interestingly, both activated clusters were enriched for 11 of these chemokines, many of which have established roles in host defense against *A. fumigatus* and other IFIs[7,48–54]. Upon arrival in the lung, the functional activity of recruited myeloid cells is regulated by cytokines such CSF1 (macrophage colony-stimulating factor) and CSF3 (granulocyte colony stimulating factor), both of which were enriched in the activated fibroblasts clusters. Immune cell activation is also accomplished by lipid mediators such as the prostaglandins[55]. DEGs involved in prostaglandin synthesis were present in both activated clusters, indicating that activated fibroblasts share cytokine- and eicosanoid-mediated signaling to modulate the immune system. In addition to cytokines, these activated alveolar fibroblasts were enriched for receptors for 25 different cytokine and prostaglandin ligands, indicating that the communication between fibroblasts and the immune system is bidirectional.

Pattern recognition receptors (PRRs) are a class of receptors on cells of the innate immune system that are on the front lines of innate immune cell recognition, binding to pathogen-associated molecular patterns (PAMPs) on microbial surfaces and triggering downstream immune activity[47]. Both activated fibroblasts clusters were enriched for PRRs, suggesting that fibroblast activation would enhance the ability of these cells to recognize microbial pathogens (Data S4). PRRs identified in the clusters included the cell surface Toll-like receptors TLR-2 and TLR-4, the intracellular sensors NOD1 and NLRC3, and the secreted PRRs that include the galectin family of lectins and pentraxin-3 (PTX3)[56–60].

By day 7 post-inoculation, the number of cells in the activated alveolar fibroblast cluster was dramatically reduced, coinciding with the appearance of another *A. fumigatus*-specific cluster that included DEGs encoding broad resident fibroblast markers *Tcf21* and *Pdgfrα*, as well as the resident alveolar fibroblast markers *Scube2*, *Npnt*, *Ces1d* and *Inmt* (Fig. 7D–E, right panel, green cluster and Table 1).

This suggests that activated alveolar fibroblasts are beginning to deactivate by day 7, indicating a progressive return to a resident alveolar fibroblast state (Fig. 7E, arrows highlight the proposed trajectory). Similarly, by day 7 the activated peribronchial fibroblast population was no longer evident (Fig. 7D–E), while the resident peribronchial fibroblast cluster was reconstituting (Fig. 7E, arrows highlight the proposed trajectory). A representative set of inflammatory genes previously upregulated in the activated alveolar and

https://doi.org/10.1038/s41467-026-71027-5

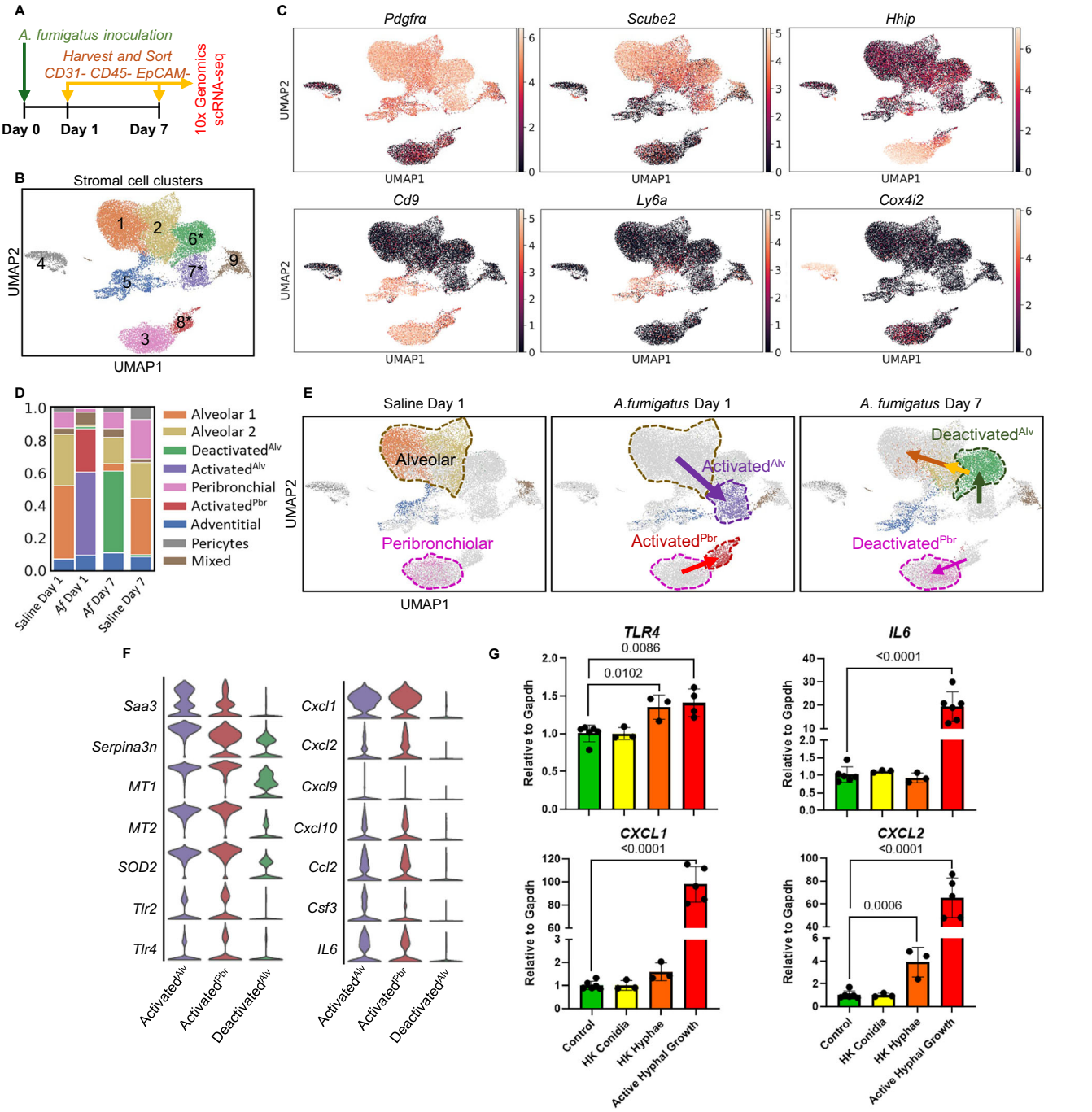

Fig. 7 | Pulmonary fibroblast sub-populations with enhanced matrix stabilizing and immunomodulatory characteristics emerge following a challenge with *A. fumigatus*. **A** Schematic representation of the experimental approach: Mice were inoculated OP with 3×10^7 conidia a saline control, and lungs were harvested at day 1 and 7 post-inoculation. Stromal cells were sorted by excluding $CD31^+$, $CD45^+$ and $EpCAM^+$ populations. **B** Uniform Manifold Approximation and Projection (UMAP) plot identified 9 stromal cell clusters (asterisks highlight clusters that are unique to the *A. fumigatus*-inoculated mice). **C** UMAP plots illustrate the expression of the indicated genes across the different clusters. The expression of these genes correlates with fibroblasts located at different anatomical sites as has been previously shown[19]: $Pdgfr\alpha^+$ and $Scube2^+$ for alveolar fibroblasts, $Hhip^+$ and $CD9^+$ for peribronchial fibroblasts, $Ly6a^+$ and $CD9^+$ for adventitial fibroblasts, and Cox4i2 for pericytes. **D** Fraction bar plot representing the relative proportion of each cluster in the four experimental groups. **E** UMAP plots highlight clusters that are uniquely present in the saline controls or on day 1 and 7 post-inoculation *A. fumigatus*. Arrows indicate the proposed trajectory based on gene expression analysis. **F** Violin plots representing inflammatory genes induced exclusively in the *A. fumigatus* induced clusters. Day 7 post-inoculation cluster reflects partial recovery to a non-inflammatory state. **G** RT-qPCR analysis of the indicated genes in primary human pulmonary fibroblast cultures stimulated for 24 h under the following *A. fumigatus* conditions: non-*A. fumigatus*-treated control (green bars), heat-killed conidia (yellow bars), heat-killed hyphae (orange bars), and viable fungus (red bars) undergoing active filamentous growth. Bars represent the mean ± SD. Dots indicate individual biological replicates (control, $n = 6$; HK conidia and HK hyphae, $n = 3$; active hyphal growth, $n = 4$; unpaired two-tailed *t*-test versus control). Source data are provided as a Source Data file.

Table 1 | Resident alveolar markers expressed by cells in the indicated clusters. Values represent the log fold change

Name	Cluster color	*Tcf21*	*Pdgfra*	*Scube2*	*Npnt*	*Ces1d*	*Inmt*
Alveolar	Orange	2.43	2.08	3.11	3.26	2.53	2.46
	Yellow	0.79	1.23	1.29	2.13	1.46	1.92
Activated alveolar	Purple	-	2.05	-	-	0.75	-
Activated peribronchial	Red	-	-	-	-	-	-
Deactivated alveolar	Green	1.94	2.11	0.6	1.27	-	1.84

activated peribronchiolar clusters was markedly downregulated in the deactivated alveolar fibroblast cluster (Fig. 7F), indicating progressive transition to a quiescent state. The return of activated fibroblast clusters to a resident phenotype is consistent with the observed histologic evidence of resolving inflammatory foci by day 7 post-inoculation with *A. fumigatus* (Fig. 1).

We conclude that exposure to an infectious threat with *A. fumigatus* triggers pulmonary stromal cells to differentiate into emergent populations of ECM-producing and immunomodulatory fibroblasts, which progressively return to a resident state as the infection resolves.

To determine whether human pulmonary fibroblasts can also adopt an inflammatory phenotype in response to *A. fumigatus*, we exposed isolated healthy primary fibroblasts to the fungus in vitro. To test their ability to directly sense fungal challenge, cells were incubated with one of four treatments: no conidia control, heat-killed conidia, heat-killed hyphae, or live conidia at a 1:50 conidia-to-fibroblast ratio (Fig. 7G). We first characterized fungal germination during co-culture, observing conidial swelling at 6 h, germling emergence by 8 h, and hyphal development at 12 h (Fig. S10A).

Temporal gene expression analysis by qPCR revealed time-dependent activation of human fibroblasts during the host-pathogen interaction. At 6 hours, inflammatory gene expression was minimal (Fig. S10B). By 8 hours, coinciding with early germination, fibroblasts upregulated *TLR4*, *CXCL1*, and *CXCL2*. This response intensified at 12 hours and peaked at 24 h, with marked induction of *IL6* (Fig. 7G). Heat-killed conidia failed to trigger activation, while heat-killed hyphae induced a modest response relative to control. The strongest activation occurred with live conidia at 24 h, highlighting the importance of fungal viability and morphological recognition in driving the immune response of human fibroblasts to *A. fumigatus*.

Together, these results demonstrate that human pulmonary fibroblasts can mount a dynamic inflammatory response to *A. fumigatus*, producing cytokines and chemokines capable of modulating immune cell recruitment and activation.

Discussion

In nature, *A. fumigatus* secretes hydrolytic enzymes for the purpose of breaking down organic material into easily metabolizable substrates. Consequently, one of the shared features of all human pulmonary infections caused by this fungus is tissue injury. Here, we provide evidence that the stromal population of the lung is an integral component of the response to fungus-mediated damage. Specifically, we demonstrate that newly synthesized collagen fibers are deposited within areas of pulmonary inflammation induced by the inhalation of *A. fumigatus* conidia (Fig. 1). By employing a lineage-tracing approach that uses *Postn* gene expression as the marker for fibroblast activation, we show that Postn^{Lin} fibroblasts emerge in the vicinity of *A. fumigatus*-induced inflammatory foci, acquiring an enlarged dendritic morphology that would increase fibroblast surface area. (Fig. 2 and S4). This morphology contrasts the thin elongated appearance of resident Pdgfrα^{Lin} fibroblast population in uninjured lung tissue. Immunohistochemical and flow cytometric analyses confirmed that *A. fumigatus*-induced Postn^{Lin} cells are part of the stromal population, and that most of them localize to the alveolar interstitium (Figs. 3 and 4), with a few residing beneath the epithelium of the conducting airways. Notably, a comparable level of activation was observed following inoculation with heat-killed conidia (Fig. S2), suggesting that the surface of a dormant inhaled conidium, coated with a hydrophobic layer of rodlet proteins[47], is sufficient to induce this response.

Using a conditional cell ablation model, we demonstrate that the absence of Postn^{Lin} cells during IPA is associated with increased pulmonary hemorrhage and fungal angioinvasion combined with an accelerated mortality rate (Fig. 6). A single dose of triamcinolone acetonide was sufficient to induce IPA and was administered 5 h after *A. fumigatus* inoculation to allow for initial host-pathogen interactions and subsequent fibroblast activation. This single-dose corticosteroid-induced immunosuppression model is known to induce an initial delay in immune responses required for IPA establishment, followed by subsequent recruitment of myeloid cells during immune reconstitution[61]. The transient immunosuppression achieved with this approach enabled the analysis of immune cell recruitment once infection was established. Strikingly, ablation of Postn^{Lin} cells in this model resulted in increased pulmonary infiltration of macrophages, neutrophils, dendritic cells, and NK cells, immune populations typically involved in the response to *A. fumigatus*[39,62]. This was associated with a hyperinflammatory response, consistent with immune-mediated tissue damage as a potential contributor to the observed increase in mortality (Fig. 6). Although immune suppression predisposes both mice and humans to IPA, hyperinflammatory responses have also been shown to worsen outcomes by accelerating mortality in mouse models[63], as well as in human cases of IPA, where clinical and radiological deterioration during neutrophil recovery is attributed to the development of an immune reconstitution syndrome[64]. These findings underscore a critical role for fibroblasts in balancing the demand for pathogen clearance with the need to mitigate collateral inflammatory damage during invasive aspergillosis. Moreover, since *A. fumigatus* proteases degrade collagen types I and III, elastin, and fibronectin in the ECM[65,66], we speculate that ablating the Postn^{Lin} lineage could also impair the timely repair of proteolytic damage. Although overall fibrosis was not affected, altered ECM turnover may compromise structural stability, thereby weakening pulmonary tissue and predisposing to fungal invasion and alveolar hemorrhage during infection.

Most of these Postn^{Lin} cells are Pdgfrα^{+}, suggesting that they arise from the resident fibroblast populations in the lung. However, pericytes, which are fibroblast-like cells located on the abluminal surface of the microvasculature[67], have also been reported to express *Postn*[26]. However, no co-labeling was observed between *A. fumigatus*–induced tdTomato^{+} Postn^{Lin} cells and the pericyte marker NG2 (Fig. 4M–O and Fig. S5H). Transcriptomic analysis of tdTomato^{+} cells by bulk RNA-seq revealed a fibrotic profile typically associated with activated fibroblasts and myofibroblasts[16] (Fig. 5). Additionally, despite basal *Postn* expression in pericytes under steady-state conditions, we detected minimal-to-no tdTomato expression in the lungs of mice treated with tamoxifen alone (Fig. 2C) or after mock inoculation with saline in the presence of tamoxifen (Fig. 2F), indicating that the cells targeted in our model are primarily de novo activated fibroblasts. We hypothesize that although pericytes may express *Postn* at baseline, their expression level is insufficient to drive Cre-mediated recombination. Supporting this, vascular permeability remained unchanged in DTA

mice (Fig S8). Since loss of pericytes would be expected to alter microvascular homeostasis[67], our finding that vascular permeability was unchanged in DTA suggests that pericytes are largely unaffected in this model.

We employed scRNA-seq to gain insight into the emergence of fibroblast heterogeneity in response to *A. fumigatus*. One of the most striking findings was the transient appearance of two clusters of cells that were unique to mice inoculated with *A. fumigatus*. These clusters were enriched in collagen fiber synthetic genes, encoding both collagen structural proteins and the oxidase and hydroxylase enzymes involved in their synthesis (P4ha2, P4ha3, Plod2, Lox, Loxl1, Loxl2). Col1a1 is the most abundant collagen and was enriched in resident alveolar fibroblasts. However, it was not enriched in the activated fibroblast clusters, which instead expressed a unique array of collagen genes (Data S4). This suggests that *A. fumigatus* triggers stromal fibroblasts to switch to the synthesis of a different set of collagens that are necessary for expansion and/or repair of the ECM. The activated alveolar fibroblast population was notably enriched in elastin and fibrillin genes, which synergize to confer both tensile strength and elasticity to lung tissue[68]. In addition, fibrillin is indirectly involved in the regulation of TGFβ activation and fibrogenesis through its interaction with latent TGFβ binding proteins[69].

It is important to note that a distinct Postn^{+} fibroblast cluster was not detected by scRNA-seq at Day 1 and Day 7 post inoculation, despite the presence of tdTomato^{+} cells in Postn^{Lin} (Figs. 2–5) mice. Consequently, transcriptional profiling of Postn^{Lin} cells was performed using bulk RNA sequencing which showed *Postn* expression (Fig. 5). Similarly, a recent scRNA-seq study interrogating the collagen-producing cells in the lung identified a subpopulation that emerges in the context of fibrotic lung disease and was characterized by expression of the collagen triple helix repeat containing-1 gene (*Cthrc1*) and *Postn*[26]. Consistent with this, we found *Cthrc1* among the top differentially expressed genes in our bulk RNA-seq analysis of Postn^{Lin} cells, but it was not detected in activated clusters captured by our scRNA-seq dataset. This discrepancy likely reflects an enrichment for high Postn-expressing cells in the bulk RNA-seq dataset (Fig. 5D), whereas Cthrc1^{+} fibroblasts may be underrepresented within the broader stromal populations captured by scRNA-seq. We propose that fibroblasts in healthy lungs are primed to respond to the daily inhalation of low levels of conidia, resulting in a moderate and transient induction of *Postn* without the need for expansion and activation that could lead to inflammatory damage.

Emerging data shows that fibroblasts have the capacity to influence inflammatory processes[70,71]. Our data support this, showing that fibroblasts activated by *A. fumigatus* upregulate the expression of cytokines and chemokines, most of which are pro-inflammatory. In addition, the enrichment of numerous cytokine receptors (Data S4) indicates that fibroblasts and immune cells engage in reciprocal communication to influence the outcome of infection. Similar transcriptional changes have been observed in COVID-19 patients[72], where fibroblasts exhibit upregulated expression of inflammatory mediators such as IL6, CXCL2, CCL2, and CSF3, mirroring the gene expression profile detected in our RNA-seq analysis (Fig. 7F). Furthermore, the emergence of inflammatory fibroblast subsets has also been reported in human idiopathic pulmonary fibrosis samples[26], underscoring a conserved pattern of fibroblast differentiation in response to tissue injury or infection. Our studies reveal that pulmonary fibroblasts may also play a direct role in pathogen recognition since the expression of cell surface, intracellular, and secreted PRRs is enhanced during activation. PTX3 is a secreted PRR that is particularly relevant to host defense against *A. fumigatus* since it functions as an opsonin with antifungal activity, and mice lacking PTX3 have increased susceptibility to IPA that can be countered by exogenous administration of PTX3[59,60,73]. In addition, we observed upregulation of the cell surface PRRs TLR-2 and TLR-4, which recognize swollen conidia, germlings, and hyphal forms of *A. fumigatus*[47]. Although these immune functions are relevant to immune protection against *A. fumigatus*, the mechanisms involved have broad specificity that would also be protective against different pathogens. It will be of considerable interest in future studies to determine whether enhanced immunomodulatory activity is a generalized response of fibroblasts to infection or whether fibroblasts can tailor their response to a specific pathogen.

Despite these major changes in gene expression, the activated fibroblast clusters were not permanent; both showed evidence of deactivation coinciding with fungal clearance and the progressive resolution of inflammatory cell foci in the lung (Fig. 1 and S1). Taking together, these in vivo studies challenge the traditional view of fibroblasts as passive bystanders involved on tissue homeostasis and repair, instead revealing them as active participants in lung protection. Through the transient induction of immunomodulatory and ECM-preserving functions, fibroblasts help mitigate the tissue damage associated with a pulmonary infection with *A. fumigatus*. These findings may offer a foundation for future targeted therapeutic strategies aimed at optimizing pathogen clearance while mitigating inflammation-mediated tissue damage.

Methods

Animal procedures

All mouse studies were conducted in accordance with the Guide for the Care and Use of Laboratory Animals of the National Research Council. The animal use protocol (20-09-09-02) was approved by the Institutional Animal Care and Use Committee (IACUC) at the University of Cincinnati.

Adult mice (12–16 weeks of age) were sex- and age-matched within experiments, cohoused, and subjected to identical treatment and infection protocols. No sex-specific differences were detected. A stock solution of Tamoxifen at 20 mg/mL (Chemodex, T0200) was prepared in a solution of 10% absolute ethanol and 90% olive oil. A dose of 5 mg per 30 g body weight was administered via gavage one day prior to *A. fumigatus* inoculation. TAM citrate-infused chow (400 mg/Kg; Inotiv TD130860) was subsequently provided to the mice for the duration of the experiment. For inoculation of conidia, 0.04 mL of a saline suspension containing 3×10^7 *A. fumigatus* conidia (unless otherwise stated) was administered by the oropharyngeal route, as previously described[74]. Control mice were inoculated with saline. To induce invasive aspergillosis, mice were immunosuppressed by subcutaneous injection of a single dose of triamcinolone acetonide (40 mg/kg body weight)[75]. Survival was monitored for 14 days until mice met pre-specified IACUC-approved early removal criteria.

Mouse lines

Rosa26-tdTomato (B6.Cg-*Gt(rosa)26Sor*$^{tm14(CAG-tdTomato)Hze}$/J; JAX Strain #:007914), Rosa26-DTA (B6.129S6(Cg)-*Gt(ROSA))26Sor*$^{tm1(DTAJpmb}$/J; JAX Strain #:032087), Pdgfrα-CreERT2 (B6.129S-*Pdgfra*$^{tm1.1(cre/ERT2)Blh}$/J; JAX Strain #:032770), and Pdgfrα-eGFP (B6.129S4-*Pdgfra*$^{tm11(EGFP)Sor}$/J; JAX Strain #:007669) mice were purchased from The Jackson Laboratory. *PostnMerCreMer* (*Postn*^{MCM}) (B6.129S-Postntm2.1(cre/Esr1*)Jmol/J; JAX Strain #:029645) mice were generated as previously described[16]. *Postn*^{MCM} and Pdgfrα-Cre mice were crossed with a Rosa26-tdTomato mouse line to enable reporter expression upon TAM-induced Cre recombination in *Postn*- or *Pdgfra*-expressing cells. Similarly, *Postn*^{MCM} mice were crossed with Rosa26-DTA mice to induce specific ablation of *Postn*-expressing cells in the presence of TAM. Heterozygous *Postn*^{MCM} and Pdgfrα-Cre mice were utilized for experiments to retain expression of the native protein, whereas homozygous Rosa26-tdTomato and Rosa26-DTA mice were used to enhance recombination efficiency. Both lineage-tracing (Postn$^{MCM/+}$; R26-tdTomato) and Cre-negative (R26-DTA) littermate mice were used as controls throughout the study. For fungal dose finding studies, we used C57BL/6 J mice in addition to our genetic models. All strains were backcrossed for more than 10

generations onto the C57BL/6 J background or purchased from JAX as already backcrossed.

Fungal strains and growth conditions

The *A. fumigatus* clinical isolate CEA10[76,77] was used throughout the study, while the clinical isolates Af293 and H237[78] were used where indicated. Conidia were harvested before each experiment from mycelia grown for 3 days at 37^{0}C on solid *Aspergillus* minimal medium (AMM) (1% [wt/vol] D-glucose, 1% [vol/vol] NH4 tartrate, 2% [vol/vol] salt solution [2.6% {wt/vol} KCl, 2.6% {wt/vol} MgSO4 heptahydrate, 7.6% {wt/vol} KH2PO4, and 5% {vol/vol} trace element solution]), then washed and resuspended in saline. When required, conidia or hyphae were inactivated by heat shock at 65 °C for 30 min. The effectiveness of heat inactivation was confirmed by plating onto the center of a plate of YG medium (0.5 yeast extract, 2% glucose) plates and confirming no surviving CFUs after 4 days of incubation at 37^{0}C. Mice were inoculated as described in *Animal Procedures*. Colony formation units (CFUs) were quantified by spreading 100 µL of serially diluted lung homogenates onto Becton Dickinson (BD) inhibitory mold agar (IMA). The plates were incubated for 16–24 h at 37 °C. At least 3 biological replicates were analyzed per condition.

Histology and immunohistochemistry

Harvested lungs were inflated with 4% paraformaldehyde (PFA) through the trachea using gravitational flow, fixed in PFA for 1 h at room temperature, and immersed in 30% sucrose (w/v) overnight at 4 °C. The lungs were then embedded in OCT (Fisher, 23730571) and stored at −80 °C prior to cryosectioning. For immunohistochemistry, cryosections of 10 µm were soaked in blocking solution (PBS containing 0.1% TritonX-100, 1.5% goat serum, and 1% bovine serum albumin) for 30 min, followed by overnight incubation at 4 °C with the primary antibody diluted 1:100 in blocking solution. The primary antibodies used in this study were Myh11(Abcam, AB224804), EpCAM/CD326 (ThermoFisher, 14579185), CD31 (BD Biosciences, 553370), CD45 (BD Biosciences, 550539) and NG2 (Abcam, AB5320). After incubation, sections were washed with PBS and incubated in blocking solution containing a 1:500 dilution of the secondary antibody for 1 h at room temperature. The secondary antibodies used were Alexa Fluor 488-conjugated goat anti-rat (ThermoFisher, A11006) or anti-rabbit (ThermoFisher, A11008), and Alexa Fluor 647 goat anti-rat (ThermoFisher, A21247) or anti-rabbit (ThermoFisher, A21244). Sections were then washed, stained with DAPI (Sigma, D9542) for 5 min to label nuclei, and mounted on slides in mounting media (Vector Laboratories, H1700). Epifluorescence images were captured using an Olympus BX43 microscope equipped with an Olympus DP80 camera and connected to an X-Cite 120 fluorescence lamp illuminator. Confocal images were taken with a Leica Stellaris 8 Confocal Microscope. Brightness and contrast adjustments were made using FIJI for epifluorescence images or LAS X software for confocal images. Quantification studies were performed by counting the indicated number of cells in a full longitudinal section of the left lung lobe. At least three biological replicates were quantified per experiment, using two sections separated by 200 µm.

For histopathology, lungs were inflated with PFA, fixed, processed, sectioned, and imaged as described elsewhere[79]. The sections were stained with Gomori's methenamine silver (GMS), hematoxylin and eosin (HE), Masson's trichrome, or Picrosirius red. Alveolar hemorrhage was assessed using a modification of a semiquantitative histologic scoring system[80]. Each animal was scored in a blinded manner by two independent investigators, with no differences observed in scoring ratios between them. Angioinvasion was quantified by counting the number of large intrapulmonary arteries ($\geq$100 µm)[81,82] in GMS-stained sections of the left lung lobe and calculating the percentage of vessels containing fungal elements. Alveolar hemorrhage and angioinvasion were assessed in at least eight biological replicates, using two sections per replicate spaced 200 µm apart. Collagen deposition in the left lung lobe was evaluated via picrosirius red staining. Multiple pictures were taken at 100-fold of magnification and quantified by ImageJ v1.54q (National Institute of Health, USA). Briefly, measure the total area of sirius red positive area by color deconvolution and normalized to the total tissue area

FACS analysis and sorting

Harvested lungs were rinsed in cold PBS and placed in a C-tube (Miltenyi Biotec, 130093237) containing 5 mL of digestion buffer consisting of Dulbecco's PBS with 0.9 mM $CaCl_2$, 600 U/mL Collagenase IV (Worthington Biochemistry, LS004189), 1.2 U/mL Dispase II (Gibco, 17105041) and 30 U/mL DNase I (Sigma, D4527-10KU). The samples were incubated in a water bath at 37 °C for 35 min and processed using a MACS™ Dissociator (Miltenyi Biotec, 130-093-235). The homogenate was filtered through a 40 µm cell strainer. Blood cells were eliminated by incubating the samples with Red Cell Lysis Buffer (eBiosciences, 00430054) following the manufacturer's instructions. The remaining cells were resuspended in FACS buffer (Dulbecco's PBS with 2x Fetal Bovine Serum) and stained with the following antibodies conjugated with APC (1:100 dilution) for 30 min at room temperature: CD45 (BioLegend, 103112), CD31 (BioLegend, 102409) and EpCAM/CD326 (BioLegend, 118214). Pericytes were labeled with Alexa Fluor 647 anti-NG2 antibody (Abcam, AB283639; 1:100 dilution). Cells were washed with FACS buffer, followed by staining with the viability dye Sytox Blue (Invitrogen, S34857) or Sytox Green (Invitrogen, S34860) at a 1:500 dilution. Flow cytometry analysis was conducted using a BD LSRFortessa and sorting performed on a BD FACSAria II Fusion. Both instruments operated using the FACSDiva software. Details of the gating strategies can be found in Figs. S4 and S6.

For immune characterization, samples were washed three times in PBS before applying fixable Live/Dead Aqua stain (ThermoFisher, L34965, 1 µL/mL) at room temperature for 20 min protected from light. Samples were then washed three times in fluorescence-activated cell sorting (FACS) buffer containing DPBS (Gibco, 14190-136) with 0.09% Sodium Azide and 1% FBS. Cells were stained for CD326 RB780 (BD Biosciences, 568737, 1:400), CD31 BV711 (BioLegend, 102449, 1:300), CD140a PE-Cy7 (ThermoFisher, 25-1401-82, 1:200), CD45 AF532 (ThermoFisher, 58-0451-80, 1:1000), F4/80 eFlour 450 (ThermoFisher, 48-4801-82, 1:200), CD11b BUV661 (BD Biosciences, 612977, 1:400), Ly6G PE-Fire 810 (BioLegend, 127673, 1:200), CD170 eFlour 660 (ThermoFisher, 50-1702-82, 1:200), FceR1a APC-eFlour 780 (ThermoFisher, 47-5898-82, 1:200), I-A/I-E PerCP (BioLegend, 107624, 1:2000), CD3e RY586 (BD Biosciences, 568158, 1:800), CD45R BV570 (BioLegend, 103237, 1:3000), CD19 BUV737 (BD Biosciences, 612782, 1:400), and NK1.1 BB700 (BD Biosciences, 566502, 1:200). After incubating for 30 min at 4 °C protected from light, cells were washed and spectral flow cytometry analysis was performed using a Cytek Bioscience Aurora Spectral Analyzer with the following five laser configurations: 355, 405, 488, 561, 640 nm, and 64 detection channels. The spectral signature of unstained, live/dead aqua stained cells, and each fluorophore was calibrated for spectral unmixing with autofluorescence extraction using single color-stained compensation beads (Invitrogen, 01-3333-42), and unstained cells for autofluorescence. Single color live/dead controls were made by heat shocking lung cell suspension at 65 °C for 5 min, once cooled, dead cells mixed with a live cell suspension on ice at a 1:1 ratio. Samples were gated for debris, doublet, and dead discrimination before analysis of target populations. Flow cytometry data was generated using FlowJo v.10.10 software (BD Biosciences).

Fungal burden quantification

To quantify fungal burden, fungal DNA from mouse lung lobes was isolated using the Quick-DNA Fungal/Bacterial Miniprep Kit (Zymo Research, D6005) according to the manufacturer's instructions. DNA concentration was determined by TaqMan PCR targeting the fungal

18S ribosomal DNA using previously reported sequences[83]: forward primer, 5′-GGCCCTTAAATAGCCCGGT-3′; reverse primer, 5′-TGAGCC GATAGTCCCCCTAA-3′; and TaqMan probe, 5′-6-FAM™-AGCCAG CGGCCCGCAAATG-TAMRA™-3′. Primers and probe were synthesized by Integrated DNA Technologies (IDT). Serial 10-fold dilutions of known concentrations of fungal DNA were prepared in parallel to generate a standard curve. Each reaction consisted of 5 μL of DNA template and 15 μL of PrimeTime Gene Expression Master Mix (IDT, 1055770) containing 250 nM probe and 500 nM of each primer, for a total volume of 20 μL. All reactions were performed in triplicate on a QuantStudio™ 3 System with the following cycling conditions: 95 °C for 3 min, followed by 45 cycles of 95 °C for 15 s and 60 °C for 1 min. The resulting Ct values were used to calculate fungal genomic equivalents (GE) based on the standard curve. Total GE in each DNA extract was then normalized to lung lobe weight and expressed as GE/mg tissue.

Vascular permeability assay

To evaluate vascular leakage, mice were administered a mixture of fluorescently labeled dextrans (3 kDa, 10 kDa, 40 kDa, and 70 kDa; Thermo Fisher Scientific) via oropharyngeal instillation. Each dextran was dissolved in PBS at 2 mg/mL. Following instillation, mice were maintained for 1 h to allow systemic distribution. Blood was collected by cardiac puncture, and plasma was isolated by centrifugation. Plasma samples and 10-fold serial dilutions of the dextran cocktail (0.015–150 μg/mL) prepared in naïve mouse serum were loaded into black 96-well plates. Fluorescence was measured with a multimode plate reader using the following excitation/emission settings: 3 kDa, 400/420 nm; 10 kDa, 650/670 nm; 40 kDa, 490/520 nm; and 70 kDa, 590/620 nm. Blank serum from untreated mice was included to correct for autofluorescence. Dextran concentrations in plasma were interpolated from standard curves using linear regression.

Gene expression analysis of inflammatory mediators in pulmonary fibroblasts

A primary human pulmonary fibroblast line (PromoCell, C12360) was cultured in Fibroblast Growth Medium 2 (PromoCell, C23020) according to the manufacturer's instructions. Cells were passaged 5–6 times and treated with *Aspergillus fumigatus* once they reached about 70% confluency. Cells were inoculated at an MOI of 10 (10 conidia per cell), except when analyzing the effect of active hyphal growth, where a lower MOI of 0.02 (1 conidium per 50 cells) was used to maintain monolayer integrity over 24 h. The RNA was isolated using a NucleoSpin RNA mini kit (Macherey-Nagel, 740955.250) according to the manufacturer's instructions, and treated with DNase I (Milipore Sigma, D7291). cDNA was synthesized using the iScript Reverse Transcription Supermix (Bio-Rad, 1708841). Gene expression was quantified with iTaq Universal SYBR Green Supermix (Bio-Rad, 1725124) on a QuantStudio™ 3 System using the following primers (5′–3′):: GAPDH-F, GAAGGTGAAGGTCGGAGT; GAPDH-R, GAAGATGGTGATGGGATTTC; IL-6-F, GGTACATCCTCGACGGCATCT; IL-6-R, GTGCCTCTTTGC TGCTTTCAC; CXCL2-F, GCTTGTCTCAACCCCGCATC; CXCL2-R, TGGATTTGCCATTTTTCAGCATCTT; CXCL1-F, GCGCCCAAACCGAA GTCATA; CXCL1-R, ATGGGGGATGCAGGATTGAG; TLR4-F, CAGAGTTT CCTGCAATGGATCA; TLR4-R, TGCTTATCTGAAGGTGTTGCACAT. All reactions were performed at least three times with the following cycling conditions: 95 °C for 20 s, followed by 40 cycles of 95 °C for 3 s and 60 °C for 30 s. Gene expression was normalized to the GAPDH expression and presented as fold-change in transcript levels relative to non–*A. fumigatus*-treated controls.

RNA sequencing and analysis

For bulk RNAseq analysis, Postn^{Lin} or Pdgfrα-GFP cells were sorted, and the RNA isolated using an RNeasy Plus Micro Kit (Qiagen, 74034) according to the manufacturer's instructions. RNA integrity was confirmed using the RNA 6000 Pico Kit on an Agilent 2100 Bioanalyzer before sequencing. The cDNA was amplified with the Ovation RNA-Seq System v2 (Tecan Genomics), and libraries were prepared using the Nextera XT DNA Library Preparation Kit (Illumina). Sequencing was performed on a NovaSeq 6000 SP v1.5 (200 cycles), yielding 100 bp paired-end reads with a sequencing depth of 30 million reads per sample. Fastq files from each sample were merged, and quality control of the sequencing reads was conducted. Adapters sequences were trimmed before further analysis. Gene expression analysis was carried out using the *Mus musculus* reference genome GRCm39 (mm39) in CLC Genomics Workbench (Qiagen). Differential expression was assessed between Postn^{Lin} cells treated with *A. fumigatus* and Pdgfrα-GFP cells treated with saline with a statistical cutoff of a Bonferroni-adjusted P-value ≤ 0.05. Gene ontology (GO) enrichment analysis was performed using the NIH DAVID Bioinformatics Functional Annotation Tool (https://david.ncifcrf.gov) applying a statistical threshold of FDR P-value ≤ 0.01 and ≥ 5 total genes per GO term. GO enrichment and volcano plots were created using RStudio (version 2024.04.2 + 764) on macOS.

For single-cell RNAseq analysis, sorted pulmonary stromal cells (negative for CD45, CD31 and EpCAM) were collected in a tube containing DMEM (Corning, 10013CV) with 10% FBS at a concentration of 100 cells/μL. The single-cell RNA-Seq assay was performed according to the manufacturer's instructions (Chromium Next GEM Single Cell 3′ Reagent Kits v3.1 (Dual Index), 10x Genomics). Briefly, cells were resuspended in the master mix and loaded together with partitioning oil and gel beads into the chip to generate a gel bead-in-emulsion (GEM). The poly-A RNA from the cell lysate contained in every GEM was reverse transcribed into cDNA, adding an Illumina TruSeq R1 primer sequence, Unique Molecular Identifier (UMI) and the 10x Barcode. The cell barcoded molecules were then cleaned up with Silane DynaBeads and amplified using 14 PCR cycles. Next, full-length, barcoded cDNA was then enzymatically fragmented, sized-selected, adapter-ligated, and amplified for library construction. During the library construction, P5, P7, i7 and i5 sample indexes, and TruSeq Read 2 were added. Samples were pooled and run on the NovaSeq 6000 sequencer with a S4 flow cell using the following sequencing parameters: R1: 28 cycles, i7: 10 cycles, i5: 10 cycles, R2: 90 cycles.

The 10x scRNA-seq data were preprocessed using Cell Ranger software (7.0.0). We used the 'mkfastq', 'count' and 'aggr' commands to process the 10x scRNA-seq output into one cell by gene expression count matrix using default parameters. scRNA-seq data analysis was performed with the Scanpy (1.9.0) package in Python (https://genomebiology.biomedcentral.com/articles/10.1186/s13059-017-1382-0). Genes expressed in fewer than three cells were removed from further analysis. Cells expressing less than 100 and more than 7000 genes were also removed from further analysis. In addition, cells with a high (≥ 10%) mitochondrial genome transcript ratio were removed. For downstream analysis, we used count per million (CPM) normalization to control for library size differences in cells and transformed those into log (CPM + 1) values. After normalization, the data were then *z*-score normalized for each gene across all cells. We then used the following commands, tl.pca', 'pp.neighbors' and 'tl.leiden, in Scanpy to partition the single cells into clusters. Differential expression analysis was done using the Wilcoxon rank sum test at the single cell level.

Statistics & Reproducibility

All experiments were repeated at least three times with similar results. Independent biological replicates are specified in the corresponding figure legends. No statistical method was used to predetermine sample size. Sample sizes were selected based on prior experience with the experimental models employed and on standards commonly used in the field to ensure reproducibility and feasibility. Outliers in gene expression and flow cytometry analyses were excluded based on

variability. Repeated experiments confirmed the reproducibility and reliability of the data. The experiments were not randomized. The investigators were not blinded to allocation during experiments and outcome assessment. Statistical data analysis was performed using Microsoft Excel 365 and GraphPad Prism v10.3.1.

Reporting summary

Further information on research design is available in the Nature Portfolio Reporting Summary linked to this article.

Data availability

The raw scRNA-seq datasets generated for this study have been deposited in the Gene Expression Omnibus (GEO)[84] with the accession numbers GSE284270 and GSE284713. Processed sequencing data are provided in the Supplementary Information (Data S1-5). All source data supporting the findings of this study are provided with the paper. Source data are provided with this paper.

References

1. Anees-Hill, S., Douglas, P., Pashley, C. H., Hansell, A. & Marczylo, E. L. A systematic review of outdoor airborne fungal spore seasonality across Europe and the implications for health. *Sci. Total Environ.* **818**, 151716 (2022).
2. Earle, K. et al. Pathogenicity and virulence of *Aspergillus fumigatus*. *Virulence* **14**, 2172264 (2023).
3. Shlezinger, N. et al. Sterilizing immunity in the lung relies on targeting fungal apoptosis-like programmed cell death. *Science (1979)* **357**, 1037–1041 (2017).
4. Okaa, U. J. et al. *Aspergillus fumigatus* drives tissue damage via iterative assaults upon mucosal integrity and immune homeostasis. *Infect. Immun.* **91**, e0033322 (2023).
5. Evans, T. J., Lawal, A., Kosmidis, C. & Denning, D. W. Chronic pulmonary aspergillosis: clinical presentation and management. *Semin Respir. Crit. Care Med* **45**, 088–101 (2024).
6. Lockhart, S. R., Chowdhary, A. & Gold, J. A. W. The rapid emergence of antifungal-resistant human-pathogenic fungi. *Nat. Rev. Microbiol* **21**, 818–832 (2023).
7. Guo, Y. et al. During aspergillus infection, monocyte-derived DCs, neutrophils, and plasmacytoid DCs enhance innate immune defense through CXCR3-dependent crosstalk. *Cell Host Microbe* **28**, 104–116.e4 (2020).
8. Espinosa, V. et al. Inflammatory monocytes orchestrate innate antifungal immunity in the lung. *PLoS Pathog.* **10**, e1003940 (2014).
9. Bonnett, C. R., Cornish, E. J., Harmsen, A. G. & Burritt, J. B. Early neutrophil recruitment and aggregation in the murine lung inhibit germination of *Aspergillus fumigatus* conidia. *Infect. Immun.* **74**, 6528–6539 (2006).
10. Lendahl, U., Muhl, L. & Betsholtz, C. Identification, discrimination and heterogeneity of fibroblasts. *Nat. Commun.* **13**, 3409 (2022).
11. Muhl, L. et al. Single-cell analysis uncovers fibroblast heterogeneity and criteria for fibroblast and mural cell identification and discrimination. *Nat. Commun.* **11**, 3953 (2020).
12. Plikus, M. V. et al. Fibroblasts: origins, definitions, and functions in health and disease. *Cell* **184**, 3852–3872 (2021).
13. Gil, H. et al. Defining the timeline of periostin upregulation in cardiac fibrosis following acute myocardial infarction in mice. *Sci. Rep.* **12**, 21863 (2022).
14. Ackerman, J. E. et al. Identification of Periostin as a critical niche for myofibroblast dynamics and fibrosis during tendon healing. *Matrix Biol.* **125**, 59–72 (2024).
15. Snider, P. et al. Origin of cardiac fibroblasts and the role of periostin. *Circ. Res* **105**, 934–947 (2009).
16. Kanisicak, O. et al. Genetic lineage tracing defines myofibroblast origin and function in the injured heart. *Nat. Commun.* **7**, 12260 (2016).
17. Bergamini, G. et al. Mouse pneumonia model by Acinetobacter baumannii multidrug resistant strains: comparison between intranasal inoculation, intratracheal instillation and oropharyngeal aspiration techniques. *PLoS One* **16**, e0260627 (2021).
18. Hohl, T. M. Immune responses to invasive aspergillosis: new understanding and therapeutic opportunities. *Curr. Opin. Infect. Dis.* **30**, 364–371 (2017).
19. Tsukui, T. et al. Collagen-producing lung cell atlas identifies multiple subsets with distinct localization and relevance to fibrosis. *Nat. Commun.* **11**, 1920 (2020).
20. Crnkovic, S. et al. Resident cell lineages are preserved in pulmonary vascular remodeling. *J. Pathol.* **244**, 485–498 (2018).
21. Klinghoffer, R. A., Hamilton, T. G., Hoch, R. & Soriano, P. An allelic series at the PDGFαR locus indicates unequal contributions of distinct signaling pathways during development. *Dev. Cell* **2**, 103–113 (2002).
22. Green, J., Endale, M., Auer, H. & Perl, A.-K. T. Diversity of interstitial lung fibroblasts is regulated by platelet-derived growth factor receptor α kinase activity. *Am. J. Respir. Cell Mol. Biol.* **54**, 532–545 (2016).
23. Zhang, X. et al. Dissecting pulmonary fibroblasts heterogeneity in lung development, health and diseases. *Heliyon* **9**, e19428 (2023).
24. Bignold, R. E. & Johnson, J. R. Matricellular protein periostin promotes pericyte migration in fibrotic airways. *Front. allergy* **2**, 786034 (2021).
25. Ozerdem, U., Grako, K. A., Dahlin-Huppe, K., Monosov, E. & Stallcup, W. B. NG2 proteoglycan is expressed exclusively by mural cells during vascular morphogenesis. *Dev. Dyn.* **222**, 218–227 (2001).
26. Tsukui, T., Wolters, P. J. & Sheppard, D. Alveolar fibroblast lineage orchestrates lung inflammation and fibrosis. *Nature* **631**, 627–634 (2024).
27. Ge, C. et al. Demethyleneberberine alleviates pulmonary fibrosis through disruption of USP11 deubiquitinating GREM1. *Pharmaceuticals* **17**, 279 (2024).
28. Shi, X. et al. GREM1/PPP2R3A expression in heterogeneous fibroblasts initiates pulmonary fibrosis. *Cell Biosci.* **12**, 123 (2022).
29. Peyser, R. et al. Defining the activated fibroblast population in lung fibrosis using single-cell sequencing. *Am. J. Respir. Cell Mol. Biol.* **61**, 74–85 (2019).
30. Strobel, B. et al. Time and phenotype-dependent transcriptome analysis in AAV-TGFβ1 and Bleomycin-induced lung fibrosis models. *Sci. Rep.* **12**, 12190 (2022).
31. Buechler, M. B. et al. Cross-tissue organization of the fibroblast lineage. *Nature* **593**, 575–579 (2021).
32. Toriumi, K. et al. LRRC15 expression indicates high level of stemness regulated by TWIST1 in mesenchymal stem cells. *iScience* **26**, 106946 (2023).
33. Krishnamurty, A. T. et al. LRRC15+ myofibroblasts dictate the stromal setpoint to suppress tumour immunity. *Nature* **611**, 148–154 (2022).
34. Ivanova, A. et al. In vivo genetic ablation by Cre-mediated expression of diphtheria toxin fragment A. *Genesis* **43**, 129–135 (2005).
35. Feng, X. et al. HacA-independent functions of the ER stress sensor IreA synergize with the canonical UPR to influence virulence traits in *Aspergillus fumigatus*. *PLoS Pathog.* **7**, e1002330 (2011).
36. Feil, R., Wagner, J., Metzger, D. & Chambon, P. Regulation of cre recombinase activity by mutated estrogen receptor ligand-binding domains. *Biochem Biophys. Res. Commun.* **237**, 752–757 (1997).
37. Vanhecke, D., Bugada, V., Steiner, R., Polić, B. & Buch, T. Refined tamoxifen administration in mice by encouraging voluntary consumption of palatable formulations. *Lab Anim. (NY)* **53**, 205–214 (2024).
38. Kuwabara, J. T. et al. Consequences of PDGFRα+ fibroblast reduction in adult murine hearts. *Elife* **11**, 69854 (2022).

39. van de Veerdonk, F. L., Gresnigt, M. S., Romani, L., Netea, M. G. & Latgé, J.-P. *Aspergillus fumigatus* morphology and dynamic host interactions. *Nat. Rev. Microbiol.* **15**, 661–674 (2017).
40. Latgé, J.-P. & Chamilos, G. *Aspergillus fumigatus* and Aspergillosis in 2019. *Clin. Microbiol. Rev.* **33**, e00140-18 (2019).
41. Sullivan, B. N., Baggett, M. A., Guillory, C., Jones, M. & Steele, C. Neuroimmune responses in a new experimental animal model of cerebral Aspergillosis. *mBio* **13**, e0225422 (2022).
42. Massagué, J. & Sheppard, D. TGF-β signaling in health and disease. *Cell* **186**, 4007–4037 (2023).
43. Onursal, C., Dick, E., Angelidis, I., Schiller, H. B. & Staab-Weijnitz, C. A. Collagen biosynthesis, processing, and maturation in lung ageing. *Front Med (Lausanne)* **8**, 593874 (2021).
44. White, E. S. Lung extracellular matrix and fibroblast function. *Ann. Am. Thorac. Soc.* **12**, S30–S33 (2015).
45. Hendrix, A. Y. & Kheradmand, F. The role of matrix metalloproteinases in development, repair, and destruction of the lungs. in *Progress in Molecular Biology and Translational Science* vol. 148 1–29 (Prog Mol Biol Transl Sci, 2017).
46. Liu, T., Gonzalez De Los Santos, F., Hirsch, M., Wu, Z. & Phan, S. H. Noncanonical Wnt signaling promotes myofibroblast differentiation in pulmonary fibrosis. *Am. J. Respir. Cell Mol. Biol.* **65**, 489–499 (2021).
47. Shankar, J., Thakur, R., Clemons, K. V. & Stevens, D. A. Interplay of cytokines and chemokines in Aspergillosis. *J. Fungi* **10**, 251 (2024).
48. Buckland, K. F. et al. Triggering receptor expressed on myeloid cells-1 (TREM-1) modulates immune responses to *Aspergillus fumigatus* during fungal asthma in mice. *Immunol. Invest* **40**, 692–722 (2011).
49. Delhaes, L., Frealle, E. & Pinel, C. Serum markers for allergic bronchopulmonary aspergillosis in cystic fibrosis: state of the art and further challenges. *Med Mycol.* **48**, S77–S87 (2010).
50. Hogaboam, C. M. et al. Immunomodulatory role of C10 Chemokine In A Murine Model Of Allergic Bronchopulmonary Aspergillosis. *J. Immunol.* **162**, 6071–6079 (1999).
51. Su, H. et al. Kinetic host defense of the mice infected with *Aspergillus Fumigatus*. *Future Microbiol* **14**, 705–716 (2019).
52. Dietschmann, A. et al. Phosphatidylinositol 3-kinase (PI3K) orchestrates *Aspergillus fumigatus*-induced eosinophil activation independently of canonical toll-like receptor (TLR)/C-type-lectin receptor (CLR) signaling. *mBio* **13**, e0123922 (2022).
53. Jhingran, A. et al. Compartment-specific and sequential role of MyD88 and CARD9 in chemokine induction and innate defense during respiratory fungal infection. *PLoS Pathog.* **11**, e1004589 (2015).
54. Mehrad, B. et al. CXC chemokine receptor-2 ligands are necessary components of neutrophil-mediated host defense in invasive pulmonary Aspergillosis. *J. Immunol.* **163**, 6086–6094 (1999).
55. Martínez-Colón, G. J. & Moore, B. B. Prostaglandin E 2 as a regulator of immunity to pathogens. *Pharm. Ther.* **185**, 135–146 (2018).
56. Meier, A. et al. Toll-like receptor (TLR) 2 and TLR4 are essential for Aspergillus-induced activation of murine macrophages. *Cell Microbiol.* **5**, 561–570 (2003).
57. Gresnigt, M. S. et al. The absence of NOD1 enhances killing of *Aspergillus fumigatus* through modulation of dectin-1 expression. *Front Immunol.* **8**, 1777 (2017).
58. Eren, E., Berber, M. & Özören, N. NLRC3 protein inhibits inflammation by disrupting NALP3 inflammasome assembly via competition with the adaptor protein ASC for pro-caspase-1 binding. *J. Biol. Chem.* **292**, 12691–12701 (2017).
59. Garlanda, C. et al. Non-redundant role of the long pentraxin PTX3 in anti-fungal innate immune response. *Nature* **420**, 182–186 (2002).
60. Gaziano, R. et al. Anti- *Aspergillus fumigatus* efficacy of pentraxin 3 alone and in combination with antifungals. *Antimicrob. Agents Chemother.* **48**, 4414–4421 (2004).
61. Duong, M. et al. Kinetic study of host defense and inflammatory response to *Aspergillus fumigatus* in steroid-induced immunosuppressed mice. *J. Infect. Dis.* **178**, 1472–1482 (1998).
62. Lionakis, M. S., Drummond, R. A. & Hohl, T. M. Immune responses to human fungal pathogens and therapeutic prospects. *Nat. Rev. Immunol.* **23**, 433–452 (2023).
63. Balloy, V., Huerre, M., Latgé, J.-P. & Chignard, M. Differences in patterns of infection and inflammation for corticosteroid treatment and chemotherapy in experimental invasive pulmonary aspergillosis. *Infect. Immun.* **73**, 494–503 (2005).
64. Jung, J. et al. Immune reconstitution inflammatory syndrome in neutropenic patients with invasive pulmonary aspergillosis. *J. Infect.* **70**, 659–667 (2015).
65. Lee, J. D. & Kolattukudy, P. E. Molecular cloning of the cDNA and gene for an elastinolytic aspartic proteinase from *Aspergillus fumigatus* and evidence of its secretion by the fungus during invasion of the host lung. *Infect. Immun.* **63**, 3796–3803 (1995).
66. Ladarola, P. et al. Lung injury and degradation of extracellular matrix components by *Aspergillus fumigatus* serine proteinase. *Exp. Lung Res.* **24**, 233–251 (1998).
67. Garrison, A. T., Bignold, R. E., Wu, X. & Johnson, J. R. Pericytes: the lung-forgotten cell type. *Front Physiol.* **14**, 1150028 (2023).
68. Godwin, A. R. F. et al. The role of fibrillin and microfibril binding proteins in elastin and elastic fibre assembly. *Matrix Biol.* **84**, 17–30 (2019).
69. Lockhart-Cairns, M. P. et al. Latent TGFβ complexes are transglutaminase cross-linked to fibrillin to facilitate TGFβ activation. *Matrix Biol.* **107**, 24–39 (2022).
70. Schuster, R., Rockel, J. S., Kapoor, M. & Hinz, B. The inflammatory speech of fibroblasts. *Immunol. Rev.* **302**, 126–146 (2021).
71. Brown, M. E. et al. A novel 3D culture model of fungal keratitis to explore host-pathogen interactions within the stromal environment. *Exp. Eye Res.* **207**, 108581 (2021).
72. Wang, S. et al. A single-cell transcriptomic landscape of the lungs of patients with COVID-19. *Nat. Cell Biol.* **23**, 1314–1328 (2021).
73. Dobiáš, R. et al. Distinguishing invasive from chronic pulmonary infections: host pentraxin 3 and fungal siderophores in bronchoalveolar lavage fluids. *J. Fungi* **8**, 1194 (2022).
74. Nielsen, T. B., Yan, J., Luna, B. & Spellberg, B. Murine oropharyngeal aspiration model of ventilator-associated and hospital-acquired bacterial pneumonia. *J. Vis. Exp.* **2018**, 57672 (2018).
75. Guirao-Abad, J. P. et al. Pleiotropic effects of the P5-type ATPase SpfA on stress response networks contribute to virulence in the pathogenic mold *Aspergillus fumigatus*. *mBio* **12**, e0273521 (2021).
76. Girardin, S. E., Cuziol, C., Philpott, D. J. & Arnoult, D. The eIF2α kinase HRI in innate immunity, proteostasis, and mitochondrial stress. *FEBS J.* febs.15553 https://doi.org/10.1111/febs.15553 (2020).
77. Guirao-Abad, J. P., Weichert, M., Albee, A., Deck, K. & Askew, D. S. A human IRE1 inhibitor blocks the unfolded protein response in the pathogenic fungus *Aspergillus fumigatus* and suggests non-canonical functions within the pathway. *mSphere* **5**, e00879-20 (2020).
78. Hensel, M., Arst, H. N. Jr, Aufauvre-Brown, A. & Holden, D. W. The role of the *Aspergillus fumigatus* areA gene in invasive pulmonary aspergillosis. *Mol. Gen. Genet* **258**, 553–557 (1998).
79. Weichert, M. et al. Functional coupling between the unfolded protein response and endoplasmic Reticulum/Golgi Ca2+-ATPases promotes stress tolerance, cell wall biosynthesis, and virulence of *Aspergillus fumigatus*. *mBio* **11**, e01060–20 (2020).
80. Klopfleisch, R. Multiparametric and semiquantitative scoring systems for the evaluation of mouse model histopathology - a systematic review. *BMC Vet. Res.* **9**, 123 (2013).

81. Stenmark, K. R., Meyrick, B., Galie, N., Mooi, W. J. & McMurtry, I. F. Animal models of pulmonary arterial hypertension: the hope for etiological discovery and pharmacological cure. *Am. J. Physiol. -Lung Cell. Mol. Physiol.* **297**, L1013–L1032 (2009).
82. Xiong, M. et al. Mouse model of experimental pulmonary hypertension: lung angiogram and right heart catheterization. *Pulm. Circ.* **11**, 1–17 (2021).
83. Bowman, J. C. et al. Quantitative PCR assay to measure *Aspergillus fumigatus* burden in a murine model of disseminated aspergillosis: demonstration of efficacy of caspofungin acetate. *Antimicrob. Agents Chemother.* **45**, 3474–3481 (2001).
84. Edgar, R. Gene Expression Omnibus: NCBI gene expression and hybridization array data repository. *Nucleic Acids Res.* **30**, 207–210 (2002).

Acknowledgements

This work was supported by National Institutes of Health grant R01 R01AI159078 (D.S.A. and O.K.), R01-HL148598 (O.K.), and University of Cincinnati Department of Pathology & Laboratory Medicine Pilot Grant to J.P.G.A.; S.M.S. were supported by an NIH Training grant T32HL125204 (PIs: Molkentin and Kranias). O.K. was supported by an American Heart Association Career Development Award CDA34110117. We would like to acknowledge the assistance of the Research Flow Cytometry Facility in the Division of Rheumatology at Cincinnati Children's Hospital Medical Center.

Author contributions

Conceptualization: D.S.A., O.K., and J.P.G.A. Funding: D.S.A. and O.K. Supervision: D.S.A., O.K., and J.P.G.A.; Methodology: J.P.G.A., D.A.K. and D.S.; Data collection: J.P.G.A., D.A.K., D.S., M.O., S.M.S., B.Y.W., J.B., C.G. Data Analysis: J.P.G.A., D.A.K., D.S., B.Y.W., J.B., Y.W., M.T. Writing—original draft: D.S.A., O.K., and J.P.G.A. Writing—review & editing: all authors.

Competing interests

The authors declare no competing interests.

Additional information

Supplementary information The online version contains supplementary material available at https://doi.org/10.1038/s41467-026-71027-5.

Correspondence and requests for materials should be addressed to José P. Guirao-Abad, David S. Askew or Onur Kanisicak.

Peer review information *Nature Communications* thanks Dean Sheppard and the other, anonymous, reviewer(s) for their contribution to the peer review of this work. A peer review file is available.